$Z\gamma^*$ production in e^+e^- interactions at $\sqrt{s} = 183 - 209$ GeV

PRELIMINARY

A. Lipniacka

Fysikum, University of Stockholm

P. Bambade, G. Borisov

LAL, Orsay

M. Boonekamp

CEA, Saclay

M. E. Pol

CBPF, Rio De Janeiro

M. Begalli, L.M. Mundim

UERJ, Rio De Janeiro

A. Di Simone, E. Graziani, L.Pieri

Universitá di Roma TRE and INFN sez. Roma 3, Rome, Italy

Abstract

Measurements of $Z\gamma^*$ production are described using the data sample collected by the DELPHI detector at centre-of-mass energies ranging from 183 to 209 GeV, corresponding to an integrated luminosity of about 667 pb^{-1}. The measurements cover a wide range of the possible final state four-fermion configurations: hadronic and leptonic ($e^+e^-q\bar{q}$, $\mu^+\mu^-q\bar{q}$, $q\bar{q}\nu\bar{\nu}$), fully leptonic ($l^+l^-l'^+l'^-$) (for which also a total cross-section measurement is performed) and fully hadronic final states ($q\bar{q}q\bar{q}$, with a low mass $q\bar{q}$ pair).

Measurements of the $Z\gamma^*$ cross-section for the various final states have been compared with the Standard Model expectations and found to be consistent within the errors.

Contributed Paper for EPS 2003 (Aachen) and LP 2003 (FNAL)

1 Introduction

The study of four-fermion processes in e^+e^- interactions becomes increasingly important as the centre-of-mass energy and the corresponding luminosity increase. The main goal of such studies is to verify the Standard Model predictions and to look for, or to set limits on, possible contributions arising from mechanisms beyond the Standard Model: anomalous triple gauge couplings [1], for instance, can usually give contributions to four-fermion final states. Moreover, such processes form an important background to new particle searches, such as those for charginos, neutralinos or non-standard Higgs bosons, and deviations from the Standard Model expectations would be a signal of new physics. LEP has provided a unique opportunity to study four-fermion interactions at several energies. On-shell pair production of W [2] and Z [3] bosons has been studied extensively. The focus of this paper is the measurement of the cross-section of neutral current processes with a Z and an off-shell photon ($Z\gamma^*$ in the following). To this end, several channels were studied: $l^+l^-q\bar{q}$ ($l \equiv e, \mu$), $q\bar{q}\nu\bar{\nu}$, $l^+l^-l'^+l'^-$ ($l, l' \equiv e, \mu, \tau$) and $q\bar{q}q\bar{q}$ (with a low mass $q\bar{q}$ pair). In addition, for $l^+l^-l'^+l'^-$ final states, a measurement of the total neutral current cross-section has also been performed.

Figure 1 shows the main Feynman diagrams for four-fermion neutral current production in e^-e^+ collisions. When there are no electrons in the final state these processes are dominated by the conversion diagrams of figure 1a. This graph represents eight different diagrams, usually referred to as the NC08 diagrams, which are responsible for ZZ, $Z\gamma^*$ and $\gamma^*\gamma^*$ production. Two diagrams (usually referred to as NC02) lead to ZZ production, two to $\gamma^*\gamma^*$ and four to $Z\gamma^*$. These four $Z\gamma^*$ conversion diagrams are sketched in figure 2, and are defined as the signal to be measured in this paper, as explained below. A prominent feature of all the graphs in figure 2 is represented by the very different scale of the couplings at the Z and γ vertices, an issue which must be properly addressed by the simulation programs (see section 3). For final states with electrons, other processes, such as multiperipheral production (figure 1d) and t-channel γ exchange accompanied by Z^*/γ^*-strahlung (figure 1c), contribute significantly. In particular, the processes originating from the bremsstrahlung diagram (1c), usually referred to as Zee and γ^*ee, are an important background to the measurements with electrons presented in this paper (see sections 4 and 6). In this case interference effects of these processes with those originating from $Z\gamma^*$ can also be important and have to be taken into account.

The $Z\gamma^*$ production cross-section, which generally is in the range of a fraction of a picobarn, depends weakly on the centre-of-mass energy, but strongly on the mass of the virtual photon, reaching values above 100 pb for real γ production when integrated over all possible γ momenta. Furthermore, particles coming from the hadronisation of low mass γ^*s are preferentially produced at very small angles with respect to the beam direction. A measurement of this cross-section has thus to be performed for a specific selection of the γ^* mass and production polar angle.

Data collected by the DELPHI experiment in 1997-2000 at centre-of-mass energies from 183 to 209 GeV were used, corresponding to an integrated luminosity of about 667 pb^{-1}. Results for each channel are given in the form of a comparison of the numbers of predicted selected events with those found in data. Combination of channel results into an overall $Z\gamma^*$ cross-section is then performed. The resulting measurement is compared to the Standard Model expectation.

This paper is organized as follows. A definition of the $Z\gamma^*$ signal is given in section 2. A

short description of the detector, of the available data sets and of the simulation programs used in the analyses is given in section 3. The subsequent sections provide descriptions of the analyses used for the channels studied: $l^+l^-q\bar{q}$ (section 4), $\nu\bar{\nu}q\bar{q}$ (section 5), $l^+l^-l'^+l'^-$ (section 6, where a total cross-section measurement is also presented), and $q\bar{q}q\bar{q}$ (section 7). Finally, sections 8 and 9 summarize results and conclusions.

2 Signal definition

Two different signal definitions were adopted in the analyses presented in this paper:

- For each of the final states considered, the signal was first defined by applying the following kinematic selection on all charged fermions:

$$|cos\theta_{f^\pm}| < 0.98 \ ,$$

  where $\theta_{f^\pm}$ is the polar angle of the charged fermion with respect to the beam axis. Events with one or more charged fermions not fulfilling the previous selection were considered as background. Then, for the surviving events, the signal was defined as the $Z\gamma^*$ contribution coming from the four-fold conversion graph in figure 1a), shown more fully in figure 2. This was achieved by weighting generated events by the quantity

$$\frac{|\mathcal{M}_{Z\gamma^*}|^2}{|\mathcal{M}_{all}|^2} \ ,$$

  where $\mathcal{M}_{Z\gamma^*}$ and $\mathcal{M}_{all}$ are the matrix elements for $Z\gamma^*$ and for all fermion graphs in figure 1, respectively. Analogously, using the same weighting technique, the components obtained by weighting events by the quantities $\frac{|\mathcal{M}_{all-Z\gamma^*}|^2}{|\mathcal{M}_{all}|^2}$ and $1 - \frac{|\mathcal{M}_{Z\gamma^*}|^2}{|\mathcal{M}_{all}|^2} - \frac{|\mathcal{M}_{all-Z\gamma^*}|^2}{|\mathcal{M}_{all}|^2}$ were considered as background: these components represent the contributions arising from non-$Z\gamma^*$ four-fermion processes (including ZZ and $\gamma^*\gamma^*$, which originate from conversion diagrams too) and from the interference effects between $Z\gamma^*$ and non-$Z\gamma^*$ graphs. This signal definition will be referred to as the "Matrix Element definition" in the following.

- The second definition was agreed between the LEP Collaborations in order to combine results in a meaningful way. It is based on invariant mass cuts at generator level and explicitly avoids the difficult regions of low di-fermion masses. Depending on the final state, the following cuts were applied on invariant masses of fermion pairs and on lepton production polar angles, where present: $M_{q\bar{q}} > 10$ GeV/c^2, $M_{l^+l^-} > 5$ GeV/c^2, $|cos\theta_{l^\pm}| < 0.95$. Furthermore, it was required that only one fermion pair in the event had an invariant mass $|M_{f^+f^-} - M_Z| < 2\Gamma_Z$, where M_Z and Γ_Z are the nominal mass and width of the Z boson. This signal definition will be referred as the "LEP definition" in the rest of the paper. Only the three dominant channels in the final result combination ($\mu^+\mu^-q\bar{q}$, $e^+e^-q\bar{q}$, $q\bar{q}\nu\bar{\nu}$) were analysed using the LEP signal definition.

In the following, when not explicitly stated, it is implied that the Matrix Element signal definitionis being used.

3 Detector description and simulation

A detailed description of the DELPHI detector and a review of its performance can be found in [4,5]. For LEP2 operations, the vertex detector was upgraded [6], and a set of scintillation counters was added to veto photons in blind regions of the electromagnetic calorimetry, at polar angles around $\theta = 40°$ and $\theta = 90°$.

The integrated luminosity of 666.7 pb^{-1} collected by the DELPHI detector at centre-of-mass energy from 182.7 to 209 GeV was used in the analysis. The luminosities collected at various centre-of-mass energies are shown in table 1.

Year	$\sqrt{s}$ [GeV]	Integrated luminosity [pb^{-1}]
1997	182.7	55.0
1998	188.6	158.1
1999	191.6	25.0
1999	195.5	77.0
1999	199.5	82.0
1999	201.6	41.0
2000	205.0	81.3
2000	206.5	147.3
Total	-	666.7

Table 1: Centre-of-mass energies and integrated luminosities of the data analysed. During the year 2000, the energies reached were in the range 202-209 GeV and clustered mainly around 205 and 206.5 GeV.

During the year 2000, one sector (1/12) of the main tracking device, the Time Projection Chamber (TPC) was inactive from the beginning of September to the end of data taking, which corresponded to about a quarter of the 2000 data sample. The effect was taken into account in the detector simulation and the corresponding small change of analysis sensitivity from this period was considered in the extraction of the cross-sections.

Simulated events were produced with the DELPHI simulation program DELSIM [5] and then passed through the same reconstruction chain as the data. The generation of processes leading to four-fermion final states, mediated by charged and neutral currents, was done with WPHACT [7,8], interfaced to the PYTHIA [9] fragmentation and hadronisation model. For the charged current part, WPHACT incorporates the $O(\alpha)$ Double Pole Approximation [10,11] radiative corrections to the doubly resonant WW production diagrams via a weighting technique, with the matrix elements provided by the YFSWW generator [12]. At a general level, WPHACT performs fully massive calculations all over the phase space, includes higher order corrections and uses the package QEDPS [13] for initial state radiation. Two additional features, particularly relevant for the analyses described in this paper, were implemented in WPHACT: the study of the most suitable scale to use for α_{QED} at the γ vertices of the diagrams in figure 2, and the treatment of the hadronisation of low mass virtual photons. The first of those problems was solved in WPHACT by implementing the running of α_{QED} at the level of the event generation, thus using the value of the coupling constant corresponding to the mass of the photon propagator at the γ vertices. The second problem was addressed by interfacing WPHACT with

3

a special package [14] for the specific treatment of the hadronisation of low mass $q\bar{q}$ systems. This package provides a description of the hadronisation from the $\gamma^* \to q\bar{q}$ process in the mass region below 2 GeV/c^2 both due to the presence of hadronic resonances (with subsequent decays described by PYTHIA) and in the continuum, based on experimental e^+e^- data at low energy. This is particularly important for the $q\bar{q}\nu\bar{\nu}$ (section 5) and $q\bar{q}q\bar{q}$ (section 7) analyses, which explore the low mass $q\bar{q}$ region. Phase space cuts are applied in WPHACT and can be found in table 2 of [8]. The study of the backgrounds due to $q\bar{q}(\gamma)$, $\mu^+\mu^-(\gamma)$ and $\tau^+\tau^-(\gamma)$ production was made using the KK2f [15] model; $e^+e^-(\gamma)$ events were simulated with BHWIDE [16]. Two-photon interactions were generated using WPHACT for the regions in which the multiperipheral contribution is not dominant and using BDK [17] for the pure $\gamma\gamma$ region; PYTHIA 6.143 was used to model $\gamma\gamma$ processes with single and doubly resolved photons.

4   Study of the $l^+l^-q\bar{q}$ final state

In this section the analysis of the final state containing jets and a pair of identified muons or electrons is described. The two final state leptons in the process $e^+e^- \to l^+l^-q\bar{q}$ are typically well isolated from all other particles. This property can be used to select such events with high efficiency in both the muon and electron channels. Events with $\tau^+\tau^-$ pairs have not been considered here.

A loose hadronic preselection was first applied, requiring that the events have at least 7 charged particles and a charged energy above 0.30 $\sqrt{s}$. To suppress the radiative return to the Z the event was rejected if a photon with energy more than 60 GeV was found. The selection procedures then proceeded in a closely similar way for the $\mu^+\mu^-q\bar{q}$ and $e^+e^-q\bar{q}$ channels. In order to maximize the lepton identification efficiency, any charged particle with momentum exceeding 5 GeV/c was considered as a possible lepton candidate around which nearby photons, if present, could be clustered. This was found to be necessary to improve the energy evaluation in the presence of final state radiation, and, in case of electrons, bremsstrahlung. In the case of the $e^+e^-q\bar{q}$ channel, photons with energy between 20 GeV and 60 GeV were also considered as electron candidates in order to recover events in which the electron track was not reconstructed. Events with at least two lepton candidates of the same flavour and opposite charge were then selected. All particles except the lepton candidates were clustered into jets and a kinematic fit requiring four-momentum conservation was applied, appropriately correcting the errors on lepton energies in cases where photons had been added by the clustering procedure.

At least one of the two lepton candidates was required to satisfy strong lepton identification criteria, while softer requirements were specified for the second. Muons were considered as strongly identified if selected by the standard DELPHI muon identification package [5], based mainly on finding associated hits in the muon chambers. For soft muon identification, only kinematic and calorimetric criteria were used. Electrons were considered as strongly identified when the energy deposited in the electromagnetic calorimeter exceeded 60% of the cluster energy or 15 GeV, whichever was greater, and when the energy deposited in the hadron calorimeter was less than a specified limit. For soft electron identification, only requirements on the momentum of the charged particle in the cluster and on the energy deposited in the hadron calorimeter were used. Moreover, electron candidates originating from applying the clustering procedure around a photon

were considered as softly identified.

Two discriminating variables were then used for final event selection: P_t^{min}, the lesser of the transverse momenta of the lepton candidates with respect to their nearest jet, and the χ^2 per degree of freedom of the kinematic fit. Cuts on these variables were applied, with values depending on the final state and on the quality of the lepton identification.

4.1 Results for the Matrix Element signal definition

The distribution of the reconstructed mass of one fermion pair when the mass of the second one is within 15 GeV/c^2 of the nominal Z mass is compared with the predictions of the Standard Model in figure 3, separately for $\mu^+\mu^-q\bar{q}$ and $e^+e^-q\bar{q}$ events. In the $\mu^+\mu^-q\bar{q}$ channel the $Z\gamma^*$ contribution is clearly separated from the background component and is mostly concentrated in the region of the decay $Z \to q\bar{q}$, as expected. In the $e^+e^-q\bar{q}$ case, the distribution is flatter, indicating the presence of non-resonant diagrams. There is an accumulation in the invariant mass distribution of the e^+e^- pair in the region between 50 and 60 GeV/c^2. Various studies and comparisons with results of the other LEP experiments were performed, reaching the conclusion that the excess is most probably due to a statistical fluctuation.

The bidimensional distributions in the plane of the masses of the two fermion pairs predicted by the Standard Model are shown in figure 4, separately for $Z\gamma^*$ and background, in the two channels studied. The presence of non-resonant contributions, particularly of the type Zee and γ^*ee, is clearly visible in the $e^+e^-q\bar{q}$ case. The distributions were binned as shown graphically in figure 4, using a small number of irregularly sized bins. This allowed the regions where most of the background is concentrated to be avoided, with the exclusion of the Zee contribution, while keeping as much signal as possible. Bin sizes were chosen in order to have an approximate equipopulation of simulated events, with a finer binning in $e^+e^-q\bar{q}$ so as to follow better the more complicated structure of the background distribution. The observed and predicted numbers of events selected by this procedure at each energy point are reported in table 2.

The efficiency and purity of the selected $\mu^+\mu^-q\bar{q}$ sample were estimated to be 42.0% and 84.7%, respectively. The residual background is composed of $\mu^+\mu^-q\bar{q}$ events outside the signal definition and of contributions from other final states. Interference effects in the $\mu^+\mu^-q\bar{q}$ channel in the region considered are negligible, as they account for less than 0.1% of the $Z\gamma^*$ cross-section. There is good overall agreement between data and the Standard Model prediction in terms of number of events. The predicted composition of the background is shown in table 3.

In the $e^+e^-q\bar{q}$ channel, the purity of the selected sample is estimated to be only 49.2%, mostly because of the unavoidable Zee background, while the efficiency was evaluated to be 24.3%. Interference effects between $Z\gamma^*$ and other four-fermion processes were estimated to account for -15% and are not negligible: they are mostly concentrated in the region of $Z\gamma^*$ - Zee overlap. Despite the observed excess in the electron-positron mass region between 50 and 60 GeV/c^2, corresponding to bin 4, there is good overall agreement in terms of observed and predicted numbers of events. The predicted composition of the background is shown in table 3.

In order to disentangle the $Z\gamma^*$ from the Zee contribution more effectively, the distribution of the polar direction of emission of the e^+e^- pair was studied as a function of the reconstructed invariant mass M_{ee} in the range defined by the first five bins in figure 4.

Correlation plots are shown in figure 5 for signal and background: the distributions are well separated because in the Zee case, which dominates the background, even e^+e^- pairs of large invariant mass are emitted at low polar angles, due to the t-channel nature of the production process. The binning in figure 4 was therefore modified, as shown in figure 5, by doubling each bin, depending on whether a) the emission polar angle of the ee pair was in the barrel region ($40° < \theta_{ee} < 140°$) or in the endcap region ($\theta_{ee} < 40°$ or $\theta_{ee} > 140°$) for bins 1-5, and b) the polar angle of the direction of the emission of the hadronic system was in the barrel or in the endcap region for bins 6-7. A total of 14 bins was thus used for the $e^+e^-q\bar{q}$ cross-section measurement. This procedure resulted in an 8% reduction of the statistical error, compared to the case where only mass bins were used.

E (GeV)	$\mu^+\mu^-q\bar{q}$				$e^+e^-q\bar{q}$			
	Data	Total MC	Signal	Background	Data	Total MC	Signal	Background
182.7	8	3.4	2.9	0.5	4	3.3	1.8	1.5
188.6	8	9.3	7.8	1.5	10	9.7	4.6	5.1
191.6	0	2.1	1.9	0.2	1	1.4	0.7	0.7
195.5	2	4.1	3.5	0.6	7	4.1	2.1	2.0
199.5	4	4.4	3.7	0.7	5	4.1	2.0	2.1
201.6	3	2.1	1.8	0.3	6	2.1	1.0	1.1
205.0	4	3.9	3.3	0.6	1	4.1	2.0	2.1
206.5	6	7.4	6.2	1.2	5	7.4	3.6	3.8
Total	35	36.7	31.1	5.6	39	36.2	17.8	18.4

Table 2: Observed numbers of events in the $\mu^+\mu^-q\bar{q}$ and $e^+e^-q\bar{q}$ channels at each energy compared with the Standard Model predictions for signal and background.

Background source	$\mu^+\mu^-q\bar{q}$	$e^+e^-q\bar{q}$
WW	0.8	1.6
$q\bar{q}(\gamma)$	0.1	1.8
$\tau^+\tau^-q\bar{q}$	2.5	2.6
non-$Z\gamma^*$ $l^+l^-q\bar{q}$	2.2	18.0
Interference	< 0.001	-5.6
Total	5.6	18.4

Table 3: Composition of the background to $Z\gamma^*$ production in the $\mu^+\mu^-q\bar{q}$ and $e^+e^-q\bar{q}$ final states predicted by the Standard Model, summed over all energy points. The row labelled non-$Z\gamma^*$ $l^+l^-q\bar{q}$ shows the four-fermion neutral current contributions from processes leading to the same final state as the signal, but defined as background as described in section 1.

The value of the $Z\gamma^*$ cross-sections at each energy point was extracted by using a binned likelihood fit technique and the values were then combined to get global results, separately for $\mu^+\mu^-q\bar{q}$ and $e^+e^-q\bar{q}$. In the $\mu^+\mu^-q\bar{q}$ case, only value of the $Z\gamma^*$ contribution was varied in the fit, while all non-$Z\gamma^*$ contributions, backgrounds and interference terms were fixed to the Standard Model expectations. In the $e^+e^-q\bar{q}$ case, where the presence

of non-resonant diagrams is relevant, a two-parameter fit was performed, leaving both the $Z\gamma^*$ and the non-$Z\gamma^*$ contributions free to vary, while fixing the remaining background sources and interference terms to the Standard Model expectations. Strictly speaking, this treatment of the interference terms is not completely rigorous, as they would be expected to vary in proportion to the product of the magnitudes of the two interfering amplitudes (which are allowed to vary in the fit) times an unknown phase factor, which can be predicted only if an explicit parametrization of some Standard Model violating term is provided. As a compromise, while the interference term was kept fixed to the Standard Model expectation in the results quoted, possible systematic effects arising from this approximation were estimated; they are discussed in the next section. The ratio $R_{non-Z\gamma^*}^{e^+e^-q\bar{q}}$ of the measured to the predicted cross-section of the non-$Z\gamma^*$ contribution to $e^+e^-q\bar{q}$ was determined to be $R_{non-Z\gamma^*}^{e^+e^-q\bar{q}} = 1.35 \; {}^{+0.30}_{-0.27}$, where the error is statistical only. Figure 6 compares the data in each bin used in the fits to the $\mu^+\mu^-q\bar{q}$ and $e^+e^-q\bar{q}$ final states with the predicted values after the fit, showing the contributions from the $Z\gamma^*$ signal, from the non-$Z\gamma^*$ component of each of the final states, from the interference terms, and from the other sources of background.

These results were used to derive the combined values of the $Z\gamma^*$ cross-section, as described in section 8.

4.2 Systematic errors for the Matrix Element signal definition

Several sources of systematic errors were investigated.

Uncertainties in the lepton identification were estimated comparing semileptonic WW events selected in data and simulation using the strong lepton identification criteria. Uncertainties in signal efficiencies from the description of the kinematic observables used were evaluated comparing the P_t and χ^2 distributions in data and simulation for all $llq\bar{q}$ events selected without mass cuts. Corresponding uncertainties in background levels were evaluated by comparing samples of events selected in data and in simulation, requiring both isolated tracks not to be identified as leptons, while maintaining all the other criteria. Finally, uncertainties in the background level in the $e^+e^-q\bar{q}$ channel from fake electrons were studied with $q\bar{q}(\gamma)$ events selected in data and in simulation with purely kinematic criteria. These effects and the statistical uncertainty of simulated data yielded a combined systematic error on the efficiency to select $\mu^+\mu^-q\bar{q}$ and $e^+e^-q\bar{q}$ events of $\pm 5.0\%$, and a relative uncertainty in the background level of $\pm 15\%$.[1]

Additional errors were added arising from the fitting procedure adopted. In the $\mu^+\mu^-q\bar{q}$ channel fit results were very stable against variations of bin sizes and number of bins: even grouping all the bins together, which is equivalent to switching to a pure counting technique, did not change the final result by an appreciable amount. For $e^+e^-q\bar{q}$ various fitting possibilities were explored. First, the doubling of bins due to the use of the polar angle of the direction of emission of the e^+e^- or $q\bar{q}$ pair was switched off. Using the same binning as in the $\mu^+\mu^-q\bar{q}$ channel, the result was 7% lower; grouping all the bins together (counting technique) increased the cross-section result by 6%; decreasing the number of bins to 5 (and keeping them approximately equipopulated) changed the cross-section result by $+2\%$. Then, with the doubling of bins enabled, a one-parameter fit

---

[1]In both cases determinations were limited in accuracy by the statistics of the available samples, and should be interpreted as upper bounds.

technique was performed, leaving free only the $Z\gamma^*$ $e^+e^-q\bar{q}$ contribution. This worsened the overall quality of the fit, but left the value of the $Z\gamma^*$ cross-section almost unchanged. This is easily understood, as in the two-parameter fitting option the second parameter absorbed in a natural way the excess observed between 50 and 60 GeV/c^2. On the other hand, the one-parameter fit to $Z\gamma^*$ is dominated by the low mass bins, and the disagreement in the region of the observed excess shows up only as a worse quality of the fit. Possible systematic effects arising from the treatment of the $Z\gamma^*$ and non-$Z\gamma^*$ interference term in the fit were taken into account (see section 4). The two-parameter fitting technique was repeated and the interference term was weighted with a factor proportional to the product of the $Z\gamma^*$ and non-$Z\gamma^*$ amplitudes being fitted. This changed the cross-section result by -2%. Note, however, that this procedure neglects a possible change in the phase between the two interfering amplitudes with respect to that predicted in the Standard Model. After all these studies, a systematic uncertainty of $\pm 7\%$ was estimated for the $e^+e^-q\bar{q}$ final state.

The systematic error coming from the uncertainty of the luminosity measurement was evaluated to be $\pm 0.4\%$ both for $e^+e^-q\bar{q}$ and for $\mu^+\mu^-q\bar{q}$.

The total estimated systematic errors on the measured $Z\gamma^*$ cross-sections were $\pm 5\%$ for $\mu^+\mu^-q\bar{q}$ and $\pm 8\%$ for $e^+e^-q\bar{q}$.

4.3   Results for the LEP signal definition

The analysis described in the previous sections was repeated adopting the LEP signal definition (see section 2). Some modifications were introduced in order to take into account the fact that the mass regions below the cuts described in section 2 must now be considered as background. Two additional selections were introduced: it was required that the reconstructed mass $M_{l^+l^-}$ of the two charged leptons be larger than 4 GeV/c^2 and that the reconstructed mass of the remaining hadronic system be larger than 8 GeV/c^2. This corresponds to suppressing bin 1 in the plot of figures 4, 5 and 6 and to reducing the size of bin 4 (6) for muons (electrons) in the same figures. The other steps of the analysis were left unchanged and the same procedures were applied to evaluate the systematic errors. The results were used to derive the values of the $Z\gamma^*$ cross-section given in section 8.1. The total estimated systematic uncertainty on the measured $Z\gamma^*$ cross-section with the LEP signal definition was $\pm 10\%$ for $\mu^+\mu^-q\bar{q}$ and $\pm 15\%$ for $e^+e^-q\bar{q}$.

5   Study of the $q\bar{q}\nu\bar{\nu}$ final state

The $q\bar{q}\nu\bar{\nu}$ channel is observed in a final state topology of hadronic matter and substantial missing energy. About half of the $Z\gamma^*$ cross-section in this channel comes from the region of $q\bar{q}$ masses below 6 GeV/c^2. Thus, final states often have the characteristic signature of "monojets", with the low invariant mass hadronic system, which is the event visible mass, arising from the γ^* hadronisation and recoiling against a highly energetic $\nu\bar{\nu}$ pair which escapes detection.

5.1   Analysis with the Matrix Element signal definition

Three analyses were performed and combined. The first analysis was intended to probe the low mass region of the hadronic system, so as to be efficient for M_{γ^*} below 6 GeV/c^2,

where most of the cross-section is expected. It is denoted as the "low mass analysis" in the following. The second analysis exploited the large energy unbalance of $q\bar{q}\nu\bar{\nu}$ events, still having some efficiency in the very low mass region of the hadronic system. It is denoted as the "energy asymmetry analysis" in the following. The third analysis was intended to have better overall efficiency than the previous ones, at the expense of having very small efficiency in the low M_{γ^*} region. It is denoted as the "high efficiency analysis" in the following.

A common event preselection was defined for the three analyses, aimed mainly at reducing the backgrounds from two-photon and Bhabha events. The energy measured in the electromagnetic calorimeters was required to be less than 60 GeV in total and less than 10 GeV at polar angles below 15° and above 165°. Events with identified electrons at polar angles below 15° and above 165° were excluded; the visible energy of the event was required to exceed 15% of the centre-of-mass energy; the polar angle of the direction of the event missing momentum was required to be in the range $15° < \theta_{miss} < 165°$; and at least two charged tracks with momentum greater than 200 MeV/c were required.

An extensive use of veto counters was implemented in all three analyses: events with hits in veto counters far from energy deposits in calorimeters or reconstructed tracks were rejected. The details of the algorithms adopted are given in the following sections.

In order to increase the available statistics, no explicit lower cut on the reconstructed mass of the hadronic system was set.

The numerical values of the cuts applied to kinematic variables in the three analyses were chosen using an optimization procedure, by maximizing the product *efficiency ×ucity* of each selected sample.

5.1.1 Low mass analysis

Events with a visible mass $M_{vis} < 6$ GeV/c^2 and with visible energy E_{vis} larger than 20% of the centre-of-mass energy were selected. In addition, in order to limit the background from leptonic decays of Ws, it was required that no identified muon be present, while at most one electron was allowed in the event, and its energy was required to be less than 30 GeV. Furthermore, events with missing momentum polar direction pointing within 2° of the 40° region (which is insufficiently covered by calorimeters) were rejected. The event was then split into two hemispheres by the plane perpendicular to the thrust axis: events were rejected if there were hits in the veto counters in the hemisphere containing the direction of the missing momentum, while events with hits in the veto counters in the opposite hemisphere were accepted only if their angular separation from the closest charged track or calorimetric energy deposit was less than 20°.

When used alone, this analysis selected 10 events in data and 6.7 in the simulation, where 4.3 were signal and 2.4 were background.

5.1.2 Energy asymmetry analysis

In this analysis events were required to be strongly unbalanced in the spatial distribution of the detected reaction products. Only events with total visible energy exceeding 20% of the centre-of-mass energy were accepted. Then two hemispheres were defined by a plane perpendicular to the direction of the thrust axis, and the energy deposited by charged and neutral particles in each of them was computed. It was required that the energy in

one of the two hemispheres account for at least 99% of the total energy in the event. This was the main topological selection of the analysis and provided an implicit upper cut-off on the total visible mass of events.

Signals from veto counters were used to discard events with possible loss of energetic photons in the insensitive regions of the electromagnetic calorimetry: the same algorithm as in the low mass analysis (see section 5.1.1) was adopted.

In order to limit further the background from processes which have most of the cross-section in the forward region (mainly Bhabha and two-photon events), the cut on the polar angle direction of the missing momentum was tightened and required to lie in the range $25° < \theta < 155°$.

At this level, the background was completely dominated by the WW and $We\nu$ processes. In order to reject leptonic decays of Ws ($W \rightarrow e/\mu \ \nu$, $W \rightarrow \tau\nu$, $\tau \rightarrow e/\mu \ \nu$), events with identified muons were discarded, while events with at most one electron were kept if the energy of the electron did not exceed 25 GeV and the electron was not isolated, i.e. its angle with respect to the closest charged track was not larger than 10°.

Additional selections were implemented in order to suppress further the WW and $We\nu$ backgrounds. Part of this background arises from hadronic decays of one W, accompanied by undetected leptons coming from the decay of the other W or lost in the beam pipe (especially in the case of $We\nu$). Such events usually show larger visible mass than is expected from signal events, due to the sizeable mass of the W boson. A selection on the event visible mass was thus imposed, requiring $M_{vis} < 45$ GeV/c^2. Another important fraction of the remaining background comes from WW events with both Ws decaying to τs, $W \rightarrow \tau\nu_\tau$, with the visible decay products boosted in the same hemisphere, due to the large fraction of momentum carried by ν_τs. The signature of these events is that a few particles carry most of the visible energy and have visible mass above a few GeV/c^2. Two more selections were imposed to reject such a source of background. Events with visible mass above 5 GeV/c^2 and with more than 90% of the visible energy carried by the two most energetic particles were discarded. The remaining events were forced into two jets with the LUCLUS algorithm [18]. Events with total particle multiplicity below 11 and an angle between the two jets above 30° were rejected.

When used alone, this analysis selected 25 events in data and 29.5 in the simulation, where 17.3 were signal and 12.2 were background. Half of the background was contributed by the WW and $We\nu$ processes.

5.1.3 High efficiency analysis

In this analysis a cut on the multiplicity of charged tracks was applied, requiring it to be larger than 4. This implied that the efficiency of the analysis dropped to zero for $q\bar{q}$ masses below 2 GeV/c^2. The main topological selections were set at jet level. Jets were reconstructed using the LUCLUS algorithm and the events were forced into a two-jet configuration. An upper cut on the opening angle of the two jets was set at 78°. The parameter d_2^{join} was defined to be the value for which the event passes from a two-jet to a single jet configuration: only events with $d_2^{join} < 30$ GeV/c were retained. The acoplanarity (defined as the complement of the angle between the jets projected on the plane perpendicular to the beams) was required to be larger than 90°. Then the event was split into two hemispheres about a plane perpendicular to the thrust axis and the energy asymmetry, defined as in section 5.1.2, was required to be larger than 95%. Events with

missing mass smaller than 80 GeV/c^2 were rejected.

A further selection was imposed on the effective centre-of-mass energy of the visible system, $\sqrt{s'}$, rejecting events with $\sqrt{s'} > 80$ GeV. In the absence of initial and final state radiation, the energy and the mass of the $q\bar{q}$ system in the $Z\gamma^*$ process are related in the following way:

$$E_{q\bar{q}} = \frac{s - M_Z^2 + M_{q\bar{q}}^2}{2\sqrt{s}} \ .$$

The quantity $E_{kin} = \frac{s - M_Z^2 + M_{vis}^2}{2\sqrt{s}}$ was defined, using the visible mass of the event. It was then required that the difference between E_{kin} and the visible energy of the event did not exceed 45 GeV. This cut, and the cut on $\sqrt{s'}$ described above, were effective in suppressing the WW and $q\bar{q}(\gamma)$ backgrounds.

Hits in veto counters were accepted if their angular distance with respect to the direction of the closest jet was less than 30°, otherwise the event was rejected.

When used alone, this analysis selected 21 events in data and 20.7 in the simulation, where 13.4 were signal and 7.3 were background. Most of the background is due to WW and $We\nu$ events.

5.1.4   Results for the Matrix Element signal definition

The three analyses were combined on an event by event basis, by selecting events which passed any of the three selections. Numerical values of the cuts were optimized by maximizing the product *efficiency* × *purity* of the total selected sample (the values listed in sections 5.1.1, 5.1.2, 5.1.3 are the result of this last optimization procedure). In total, 42 events were found in data and 41.3 in the simulation (with a total overlap between the three selections of about 30%), where 23.4 were signal and 17.9 were background. The most abundant source of background was predicted to come from $We\nu$ events, which accounted for 7.9 events, mainly in the channel $q\bar{q}e\nu$ and partially in $\tau\nu e\nu$. On-shell WW processes contributed about 4 events to the background, with 2.9 of them containing at least one W decaying to $\tau\nu$. The remaining main sources of background were $q\bar{q}$ (about 2 events), $\tau\tau$ (about 2 events) and other four-fermion neutral current processes (1.1 events). Table 4 shows the numbers of signal and background events predicted by the Standard Model and the observed numbers of events in the $q\bar{q}\nu\bar{\nu}$ channel at the various centre-of-mass energies.

The average selection efficiency, as computed from the simulation, was 38.8 %, where the error is statistical only. The differential efficiency as a function of the generated mass, $M(q\bar{q})$, from the simulation is shown in figure 7. The distribution of the reconstructed visible mass, M_{vis}, for the 42 data events is shown in figure 8, which also shows the distributions for the simulated signal and background events. Good agreement is observed with the Standard Model expectations.

The value of the $Z\gamma^*$ cross-section at each energy point was extracted using a counting technique and the values were then combined to get a global result. All non-$Z\gamma^*$ contributions, backgrounds and interference terms were fixed to the Standard Model expectations. The result was used to derive a combined value for the $Z\gamma^*$ cross-section, as described in section 8.

E (GeV)	Data	Total MC	Signal	Background
182.7	3	3.5	2.3	1.2
188.6	9	10.1	6.0	4.1
191.6	1	1.3	0.9	0.4
195.5	7	4.4	2.9	1.5
199.5	6	5.2	2.9	2.3
201.6	2	2.5	1.3	1.2
205.0	9	4.9	2.6	2.3
206.5	5	9.4	4.5	4.9
Total	42	41.3	23.4	17.9

Table 4: Observed numbers of events in the $q\bar{q}\nu\bar{\nu}$ channel at each energy compared with the Standard Model predictions for signal and background.

5.1.5 Systematic errors for the Matrix Element signal definition

Various sources of systematic error were considered.

The predicted background cross-sections were varied according to the following values: $WW : \pm 2\%$, $q\bar{q} : \pm 5\%$, $We\nu : \pm 5\%$, $\tau\tau : \pm 5\%$, four-fermion neutral current processes: $\pm 5\%$. The combined effect on the cross-section measurement was estimated to amount to $\pm 2\%$, with the main contribution coming from the uncertainty on the $We\nu$ cross-section.

Uncertainties on the signal efficiency coming from the Monte Carlo generator were studied by comparing different generator models. In particular, a sample of $q\bar{q}\nu\bar{\nu}$ was generated with the EXCALIBUR [19] four-fermion generator, for masses of the hadronic system $M(q\bar{q}) > 2$ GeV/c^2, and with a modified version of the KORALW [20] program for $M(q\bar{q}) < 2$ GeV/c^2, where a simplified hadronisation model was used, allowing only the process $\gamma^* \to \rho^0 \to \pi\pi$. The full analysis was applied to this sample and a difference of 5% in the signal efficiency was obtained. A systematic uncertainty of $\pm 5\%$ was thus conservatively ascribed to this source.

The stability of the result as a function of the applied experimental cuts was checked by varying the selections of the three analyses, first separately and then at the same time. The procedure set up to maximize the *efficiency × purity* product of the simulated sample (see section 5.1.4) was used to vary all the relevant cuts of sections 5.1.1, 5.1.2 and 5.1.3 within reasonable values: selections were accepted if the predicted *efficiency × purity* product differed by less than the statistical error of the optimum value obtained from the simulated sample used in the analysis. For each new selection signal efficiency, the background level and number of events in data were estimated and a value for the $q\bar{q}\nu\bar{\nu}$ cross-section was measured. The root mean square of the distribution of the cross-sections evaluated in this way was assumed to represent the systematic uncertainty coming from the choice of the particular set of cuts used, and amounted to $\pm 3\%$.

Another source of systematic uncertainty considered was the reliability of the simulation in correctly estimating the amount of background. As explained in section 5.1.4, the main backgrounds are WW events, with one or both Ws decaying to τ, and $We\nu$ events, with the on-shell W decaying hadronically or to $\tau\nu$. These events share the common feature of having the decaying products of one W detected on one side, and missing energy on the other side. The missing energy is due to the low angle electron typically lost in

the beam pipe in the $We\nu$ case, or to an undetected decay lepton or charged track in the WW case. Furthermore, in both topologies, additional missing energy is carried by the escaping neutrino. In order to evaluate the reliability of the simulation in estimating the efficiency to detect backgrounds in such a topology, events with features similar to that of the real analysis background were studied. In particular, WW events with one W decaying to a detected lepton (electron or muon) or to an isolated charged track, which was then artificially removed from the event, can mimic most of the WW and $We\nu$ background, with the second W playing the role of the hadronic signal. Therefore events with an isolated electron, muon or other charged particle track were selected. Identified leptons or other charged tracks were initially required to have momentum larger than 10 GeV/c and an angle with respect to the closest charged track larger than 10°. The selected candidate track was then excluded from the event and the selections in sections 5.1.1, 5.1.2 and 5.1.3 applied to the remaining system. At the end of the procedure, 142 events with an isolated muon were found in data and 135.7 in the simulation, 110 events with an isolated electron were found in data and 115.1 in the simulation, and 79 events with a single isolated charged track were found in data and 72.4 in the simulation. The distribution of the isolation angle of the selected lepton or single track after all the cuts is shown in figure 9. Good agreement between data and simulation can be observed. The dominant contributions to the events selected in this way come from semileptonic WW production, $\tau\tau$ events and, to a lesser extent, Bhabha events, and can thus be used to emulate the background to the $q\bar{q}\nu\bar{\nu}$ signal: when the isolated lepton or the charged track is excluded from the sample, the remaining system is strongly unbalanced in visible momentum and of the same topology as the background expected in the $q\bar{q}\nu\bar{\nu}$ sample. (It may be noted that the estimated contribution from the $q\bar{q}\nu\bar{\nu}$ signal to this sample is totally negligible).

The agreement between data and simulation in figure 9 was subjected to more detailed checks, for example by selecting the region of the distribution in the isolation angle of the single charged track which enriches the sample in WW events: two-fermion events preferentially populate the region of large isolation angle, being almost back to back, and their contribution can be greatly reduced with a cut at around 130°. Similarly, other checks were made for different visible mass and track multiplicity regions: in all the cases the agreement between data and Monte Carlo was good within the errors. The statistical error in the total of 331 events selected by this procedure was thus taken as an estimate of the systematic uncertainty due to the background evaluation from the simulation: this gave a contribution of $\pm 3\%$ on the cross-section measurement.

The systematic uncertainty coming from the luminosity measurement was estimated to give an error of $\pm 0.8\%$ on the cross-section measurement.

Finally, the statistical error from the limited simulated sample gave an uncertainty of $\pm 5\%$.

The total estimated systematic error on the $Z\gamma^*$ $q\bar{q}\nu\bar{\nu}$ cross-section measurement was thus estimated to be $\pm 9\%$.

5.2   Results for the LEP signal definition

The analysis described in the previous sections was used adopting the LEP signal definition (see section 2). In close analogy with section 4.3 some modifications were introduced in order to take into account the fact that the $q\bar{q}$ mass region below the cut described in section 2 must be considered as background. The low mass analysis (see section 5.1.1) was

not used. Then, in the energy asymmetry and high efficiency analyses (see sections 5.1.2 and 5.1.3, respectively), it was required that the reconstructed mass of the hadronic system be larger than 8 GeV/c^2. The other steps of the analyses were left unchanged and the same procedures were applied to evaluate the systematic errors as were used for the Matrix Element signal definition. The results obtained were used to derive the values of the $Z\gamma^*$ cross-section given in section 8.1. The total estimated systematic uncertainty on the measured $Z\gamma^*$ cross-section with the LEP signal definition was $\pm 16\%$.

6   Study of the $l^+l^-l'^+l'^-$ final state

Only the Matrix Element signal definition was used to study the $l^+l^-l'^+l'^-$ final state.

The Feynman diagrams of figure 1 give rise to six possible final states with four charged leptons: $\mu^+\mu^-\mu^+\mu^-$, $e^+e^-e^+e^-$, $\tau^+\tau^-\tau^+\tau^-$, $e^+e^-\mu^+\mu^-$, $e^+e^-\tau^+\tau^-$ and $\mu^+\mu^-\tau^+\tau^-$. These final states have a rather clean experimental signature, but do not contribute significantly to the total four-fermion production cross-section due to the low branching fraction of $Z/\gamma^* \rightarrow l^+l^-$.

The event selection was restricted to topologies with four well reconstructed charged particles with momenta larger than 2 GeV/c (henceforth called lepton candidates). Events with two additional well measured charged particles with opposite charges were allowed, provided that the pair was compatible with a photon conversion, or that the momentum of both tracks was less than 2 GeV/c. Five additional charged particles were allowed in the event if their tracks did not point to the vertex: such tracks were not considered in the following steps of the analysis. The previous selections implied that for $e^+e^-\tau^+\tau^-$, $\mu^+\mu^-\tau^+\tau^-$ and $\tau^+\tau^-\tau^+\tau^-$ events only one-prong τ decays were considered. The sum of the charges of the lepton candidates had to equal zero and the angle between the directions of any two of them had to be larger than $5°$.

The four lepton candidates had to fulfil the following additional selection criteria: the momenta of at least three of them had to be larger than 6 GeV/c, their total energy had to be larger than $0.25\sqrt{s}$ (to reject background from two-photon interactions), and the track length of at least three of the candidates had to be larger than 50 cm. Beam-gas and $\tau^+\tau^-\gamma$ events were rejected by requiring that the four lepton candidates were not all in the same hemisphere with respect to the beam direction. For data taken during 2000, in the period when one sector of the TPC was not working, a slightly more relaxed criterion for track selection was applied if the track was in that sector.

Selected events in the data were compared with simulated signal and background samples generated at the eight centre-of-mass energies. The expected numbers of events for signal and background, together with the numbers of events found in data, are shown in table 5. The overall selection efficiency is $\approx 15\%$, increasing slightly with $\sqrt{s}$. The most important contribution to the background comes from $e^+e^- \rightarrow e^+e^-q\bar{q}$ events with low $q\bar{q}$ mass. The second most important contribution is due to the $e^+e^- \rightarrow \tau^+\tau^-(\gamma)$ process. Good agreement was found between the data and the predictions of the simulation after each selection was applied sequentially.

E (GeV)	Data	Total MC	Signal	Background
182.7	3	3.90	3.45	0.45
188.6	14	12.39	10.00	2.39
191.2	1	1.82	1.62	0.20
195.5	5	5.27	4.62	0.65
199.5	8	5.97	5.15	0.82
201.6	3	2.72	2.36	0.36
205.0	7	5.32	4.79	0.53
206.5	7	9.58	8.15	1.43
Total	48	46.97	40.14	6.83

Table 5: Observed numbers of events in the $l^+l^-l'^+l'^-$ channel at each energy compared with the Standard Model predictions for signal and background.

6.1 Particle identification and final state classification

Selected events were classified into one of the six final states according to the number of identified muons, electrons and pions. A constrained fit procedure was also used to complete the identification.

Muon identification was performed by combining the standard DELPHI identification package [5] in the muon chambers with the energy deposition profile in the hadron calorimeter and the energy deposited in the electromagnetic calorimeter.

Electron identification required that there be no signal in the muon chambers and no energy deposited in the hadron calorimeter after the first layer. The energy in the electromagnetic calorimeter in a 2° cone surrounding the candidate particle was required to be larger than 1 GeV. For electrons satisfying these criteria, the momentum of the charged particle was replaced by the energy deposited in the electromagnetic calorimeter.

Pions were identified as tracks leaving an energy deposit in the electromagnetic calorimeter compatible with a minimum ionizing signal, no hits in the muon chambers and energy deposited in the layers of the hadron calorimeter compatible with the profile of a hadron shower.

The assignment of the final state proceeded as follows:

- If no e^+e^- or $\mu^+\mu^-$ pair was identified, the four particles were considered as τ decays and the final state to be $\tau^+\tau^-\tau^+\tau^-$.

- If two pairs were identified as e^+e^-, $\mu^+\mu^-$ or $\tau^+\tau^-$ $(\pi^+\pi^- + n\gamma)$, the final state was considered to be fully identified.

- If an e^+e^- or $\mu^+\mu^-$ pair was identified and the second pair had two identified particles, different from one another, the event was considered to be $e^+e^-\tau^+\tau^-$ or $\mu^+\mu^-\tau^+\tau^-$, respectively. The second pair was also designated as $\tau^+\tau^-$ if only one particle was identified and was different from the identified pair, or if neither was identified.

- If the event had 3 identified electrons or muons and one unidentified particle, two hypotheses were considered: that the 4 particles were identical or that the unidentified particle was one of a $\tau^+\tau^-$ pair.

A constrained kinematic fit was then performed on the selected events, imposing four-momentum conservation. Where more than one kinematic hypothesis could be applied to the same event, the fit with the best χ^2 per degree of freedom was selected, thus deciding the final state identification. If no acceptable hypothesis was found, further fits were tried, assuming, in addition to the four leptons, the presence of an unobserved ISR photon in the beam pipe; again, the best resulting fit was selected. The masses of the two l^+l^- pairs were then calculated from the results of the chosen fit. Figure 10 shows the distributions of the larger and smaller mass pairs in the event, obtained from the full data sample, and compares them with the predictions of the Standard Model.

The efficiencies for assigning the correct final states to the selected events were estimated from the simulation. The results are summarized in table 6, which shows the cross-talk matrix for the total expected number of events identified in each channel and the estimated purity of each $l^+l^-l'^+l'^-$ state with respect to the total $l^+l^-l'^+l'^-$ content of the selected event sample.

	true $e^+e^-e^+e^-$	true $e^+e^-\mu^+\mu^-$	true $e^+e^-\tau^+\tau^-$	true $\mu^+\mu^-\mu^+\mu^-$	true $\mu^+\mu^-\tau^+\tau^-$	true $\tau^+\tau^-\tau^+\tau^-$
$e^+e^-e^+e^-$	6.44	0.00	0.28	0.00	0.00	0.00
$e^+e^-\mu^+\mu^-$	0.00	13.80	0.28	0.00	0.14	0.01
$e^+e^-\tau^+\tau^-$	3.25	1.49	3.17	0.00	0.02	0.07
$\mu^+\mu^-\mu^+\mu^-$	0.00	0.01	0.00	2.32	0.13	0.00
$\mu^+\mu^-\tau^+\tau^-$	0.00	4.00	0.05	0.42	1.56	0.05
$\tau^+\tau^-\tau^+\tau^-$	0.41	0.49	0.63	0.02	0.17	0.19
purity (%)	64	70	72	84	77	59

Table 6: Upper rows: Cross-talk matrix for the $l^+l^-l'^+l'^-$ content of the expected event sample, estimated from the simulation. Bottom row: Estimated purity of each $l^+l^-l'^+l'^-$ state with respect to the total $l^+l^-l'^+l'^-$ content of the sample.

A negligible number of events could not be classified in any of the six final states as there was no complete *a priori* identification of the event and the constrained fit failed. Identified final states with four τ decays showed larger background than the other four-lepton channels due to lack of identification of electrons or muons, mainly in regions with poor coverage by the electromagnetic calorimetry or muon chambers, or from inefficiencies in the particle identification algorithms.

6.2   Results

The value of the $Z\gamma^*$ cross-section at each energy point was extracted using a procedure which followed closely that adopted for the $l^+l^-q\bar{q}$ channels in section 4.1. Bidimensional mass distributions were constructed in the plane of the masses of the pairs with the larger and smaller mass in the event. The distributions were binned using the same definition as the first five bins in figure 4 for the $e^+e^-q\bar{q}$ case. The number of events selected in the bins from the data was 17, while the simulation predicted 16.6: 5.5 were $Z\gamma^*$ signal, 9.6 were due to the non-$Z\gamma^*$ $l^+l^-l'^+l'^-$ contribution, 2.3 were non-$l^+l^-l'^+l'^-$ background and -0.8 represented the contribution of interference terms. Of the 17 selected data events,

1 was classified as $e^+e^-e^+e^-$, 4 as $e^+e^-\mu^+\mu^-$, 6 as $e^+e^-\tau^+\tau^-$, 1 as $\mu^+\mu^-\mu^+\mu^-$ and 5 as $\mu^+\mu^-\tau^+\tau^-$.

A two-parameter binned likelihood fit to the $Z\gamma^*$ and non-$Z\gamma^*$ $l^+l^-l'^+l'^-$ contributions was performed, fixing the remaining backgrounds and interference terms to the Standard Model expectations. These results were used to derive the combined values of the $Z\gamma^*$ cross-section, as described in section 8.

6.3   Systematic errors

Several sources of systematic uncertainties were investigated.

The main contribution to the systematic error in the track selection came from the difference between data and simulation in the number of reconstructed charged tracks. In order to estimate this uncertainty, samples of events with one selected muon, two selected muons and two muons plus one charged track were compared in data and in the simulation. From the comparison, a conservative uncertainty of $\pm 5\%$ was assigned as the systematic error from this source. For dimuon events with two reconstructed charged tracks, it was verified that the difference between data and simulation in the number of events with total charge equal to zero was of the order of 0.5%.

Systematic uncertainties originating from particle identification were also taken into account. Two pure samples of e^+e^- and $\mu^+\mu^-$ final states were selected from the data without making use of the particle identification criteria described in section 6.1 and were compared with simulated samples of the same final states. Then the identification criteria for electrons and muons were applied to both samples and the difference in the efficiencies between data and simulation was taken as a systematic error. This resulted in errors of $\pm 0.5\%$ for muons and $\pm 5\%$ for electrons. The poorer of the two estimates was also used for τs and adopted as a systematic uncertainty on the cross-section measurement.

Possible errors arising from the procedure adopted in the fits to the l^+l^- mass distribution were studied. Several checks were performed, in close analogy to those described in section 4.2. First, simulated samples of events with electrons in the final state (which receive large contributions from t-channel processes) were split into two categories, depending on whether or not the electrons were identified in the event reconstruction. The cross-sections of the two samples were measured and then combined. Secondly, a one-parameter fit to the mass distribution was performed, both on the whole selected $l^+l^-l'^+l'^-$ sample and on the two separated samples with final state electrons described above, allowing only the $Z\gamma^*$ component to vary. From the spread of the results of these additional fits, a systematic error of $\pm 7\%$ was estimated.

The error in the efficiency for selecting signal events due to the limited Monte Carlo statistics was evaluated to be $\pm 0.6\%$. The limited statistics used for the different background processes was also taken into account, as well as the theoretical uncertainties in the cross-sections, resulting in contributions of $\pm 0.06\%$ and $\pm 1.1\%$, respectively. Finally, from the determination of the luminosity, a contribution to the systematic error of $\pm 0.8\%$ was estimated.

The total estimated systematic error on the $l^+l^-l'^+l'^-$ $Z\gamma^*$ cross-section measurement was thus estimated to be $\pm 10\%$.

6.4 Measurement of the total cross-section for $l^+l^-l'^+l'^-$ production

Because of the simplicity of the topologies involved in the detection of the $l^+l^-l'^+l'^-$ final state and the low level of background present in the selected data samples, these states are signature to many processes which will be studied by the next generation of colliders, such as the searches for Higgs production and for processes beyond the Standard Model. Therefore we report a total cross-section measurement for $l^+l^-l'^+l'^-$ production, in addition to the study of $Z\gamma^*$ production in the four-lepton topology described in section 6.2 above.

The total cross-section was calculated taking into account the background and selection efficiencies, without using particle identification:

$$\sigma = \frac{N_d - N_b}{L\epsilon} \ ,$$

where N_d is the number of events found in the data, N_b is the expected number of background events found from the simulation, L is the luminosity and ϵ the efficiency for the signal. As the cross-section does not vary too much within the energy range of LEP2, all the data and the Monte Carlo simulations for the different energies were grouped together.

The total cross-section for the $l^+l^-l'^+l'^-$ processes, within the visible region defined by $|cos\theta_l| \leq 0.98$, was found to be

$$\sigma = (0.430 \pm 0.062 \pm 0.021) \ \text{pb}$$

at a luminosity-averaged centre-of-mass energy of 197 GeV. The first error quoted is statistical; the second is the estimated systematic error, derived as described in section 6.3 above, but without including effects involving particle identification.

This result is in good agreement with the predicted cross-sections from WPHACT, which range from 0.440 pb at $\sqrt{s} = 182.7$ GeV to 0.375 pb at $\sqrt{s} = 206.5$ GeV.

7 Study of the $q\bar{q}q\bar{q}$ final state

Only the Matrix Element signal definition was used to study the $q\bar{q}q\bar{q}$ final state.

The measurement of the $Z\gamma^*$ contribution in the $q\bar{q}q\bar{q}$ channel has to deal with background processes such as $q\bar{q}(\gamma)$ and WW which have cross-sections larger by orders of magnitude than the signal. It is thus not feasible to measure the $Z\gamma^*$ cross-section in all the possible $q\bar{q}$ mass spectrum. Only a restricted region was thus considered here, for low values of the reconstructed mass of one $q\bar{q}$ pair. The signature of the process studied in this analysis is the presence of a highly energetic isolated low mass jet from the γ^* hadronisation (preferentially directed in the forward region), recoiling against a system of two (or more) jets from the hadronic Z decay. The study of the γ^* system was limited to final states with only two charged particles and an arbitrary number of neutral particles: this choice was driven by the expectation that, in the low mass region, the process $\gamma^* \to q\bar{q}$ is dominated by the hadronisation chain $\gamma^* \to \rho^0 \to \pi\pi$. Furthermore, an explicit cut on the reconstructed mass was used, as explained below in the description of the analysis. The $Z\gamma^*$ signal definition was kept the same as in the other channels studied (with no limits

on the γ^* mass); as a result, the two selection criteria mentioned above (those requiring low multiplicity and low reconstructed mass) imply a large inefficiency in the analysis of events with $\gamma^* \to q\bar{q}$ for $\gamma*$ masses above a few GeV/c^2.

The principal backgrounds arise from production of $q\bar{q}(\gamma)$, WW and final states from other four-fermion neutral current processes such as $q\bar{q}\mu^+\mu^-$, $q\bar{q}e^+e^-$ and $q\bar{q}\tau^+\tau^-$.

A preselection was applied to the data in order to select hadronic events compatible with the expected topologies. The total charged particle multiplicity was required to be larger than 20; the ratio $\sqrt{s'}/\sqrt{s}$ had to be larger than 77%, where $\sqrt{s'}$ is the reconstructed effective centre-of-mass energy; events with neutral particles with electromagnetic energy larger than 50 GeV were excluded; the missing energy of the event was required to be less than 82% of the centre-of-mass energy; and the number of identified muons was required to be less than two (to limit the background from $q\bar{q}\mu^+\mu^-$ events). Events were then clustered according to the LUCLUS [18] algorithm with the parameter d_{join} set to 6.5 GeV/c, and it was required that the number of reconstructed jets in the event be larger than two. One of the jets had to contain at least one charged particle with momentum exceeding 32 GeV/c and to have charged particle multiplicity of two, while an arbitrary number of neutral particles in the jet was accepted. The pair of charged particles was then subjected to the selections listed below. These selections were the result of an optimization process, briefly described hereafter.

- The impact parameters of the two charged particles were required to be compatible with the primary event vertex.

- The total energy of the pair was required to be larger than 63 GeV.

- The two charged particles had to be of opposite charge.

- The sum of the electromagnetic energies of the two particles was required to be less than 40% of the total energy of the pair.

- Identified muons and electrons were not allowed in the pair.

- The system recoiling against the jet containing the selected pair was forced into a two-jet configuration and the full kinematics of the three jets was completely determined by their space directions. Then the two-jet system not containing the selected pair was required to have a reconstructed mass within 11 GeV/c^2 of the nominal Z mass.

- The invariant mass of the two charged particles had to be less than 2.1 GeV/c^2.

Numerical values of the cuts were optimized by scanning the full range of the relevant discriminating variables and calculating, for each set of values, the cross-section and the quantity *efficiency × purity*. The set with the highest value of ϵp, corresponding to $\epsilon = 2.2\%$, $p = 69.4\%$ and a ratio $\frac{signal}{\sqrt{background}} = 3.3$, was chosen. The procedure selected 7 events in data and 6.94 in the simulation, of which 4.82 were signal and 2.12 were background. The main backgrounds came from WW events (1.13 events), $q\bar{q}(\gamma)$ events (0.41 events) and other four-fermion neutral current processes (0.42 events). Figure 11 compares the distribution of the reconstructed mass of the pair of selected charged tracks before the last cut with Standard Model predictions. Table 7 shows the predicted numbers

of signal and background events and the observed numbers of events in the $q\bar{q}q\bar{q}$ channel at the various centre-of-mass energies.

E (GeV)	Data	Total MC	Signal	Background
182.7	1	0.45	0.39	0.06
188.6	2	1.87	1.37	0.50
191.6	0	0.18	0.15	0.03
195.5	0	0.82	0.44	0.38
199.5	0	0.99	0.80	0.19
201.6	2	0.30	0.25	0.05
205.0	1	0.61	0.45	0.16
206.5	1	1.72	0.97	0.75
Total	7	6.94	4.82	2.12

Table 7: Observed numbers of events in the $q\bar{q}q\bar{q}$ channel at each energy compared with the Standard Model predictions for signal and background.

The value of the $Z\gamma^*$ cross-section at each energy point was extracted using a counting technique and the values were then combined to determine a global result. All non-$Z\gamma^*$ contributions, backgrounds and interference terms were fixed to the Standard Model expectations. The result was used to derive a combined value for the $Z\gamma^*$ cross-section, as described in section 8.

7.1 Systematic errors

Various sources of systematic error were considered.

The predicted background contributions from WW, $q\bar{q}(\gamma)$ and four-fermion neutral current production were varied by changing the cross-sections for these processes according to the values given in section 5.1.5: the combined effect on the cross-section measurement was estimated to amount to $\pm0.5\%$.

The statistical error corresponding to the limited simulated sample gave an uncertainty of $\pm5\%$.

The stability of the result as a function of the applied experimental cuts was checked by varying the numerical values of the analysis selections. The procedure set up to maximize the *efficiency* $\times$ *purity* product of the simulated sample (see section 7) was used to vary all the relevant cuts within reasonable limits: selections were accepted if the predicted *efficiency* $\times$ *purity* product differed by less than the statistical error of the simulated sample from the optimum value used in the analysis. For each new selection, the signal efficiency, background level and number of events in data were estimated, and a value for the cross-section was measured. The root mean square of the distribution of the cross-sections thus obtained was assumed to represent the systematic uncertainty coming from the choice of the particular set of cuts used, and amounted to $\pm15\%$.

The reliability of the simulation in reproducing the amount of background was checked by repeating the analysis selecting pairs of tracks of the same charge. The same cuts as those described in section 7 were applied, with the exclusion of the requirement on the total charge of the pair. No events were selected in data, while 0.56 were predicted by the simulation. The results are of course compatible, but to derive a numerical estimate for

20

a systematic error, the procedure was enlarged. A new selection was made by softening the cut on the invariant mass of the pair of charged tracks, which was required to be less than 10 GeV/c^2, and leaving all the other selections unchanged. This gave 3 events in data and 4.5 in the simulation, of which 3.6 were due to WW production and 0.5 to $q\bar{q}(\gamma)$ backgrounds.

A similar study was performed to check the four-fermion neutral current background, which gave a negligible contribution in the previous procedure. The selections in section 7 were repeated on data and simulation, but replacing the veto of having identified electrons or muons in the selected pair of charged tracks by the requirement that at least one of the two tracks was positively identified as a lepton (electron or muon). In addition, the cut on the invariant mass of the pair was softened to 10 GeV/c^2, as for the check described in the previous paragraph. This resulted in 8 events selected in the data and 6.9 predicted from the simulation, of which 5.7 were due to the four-fermion neutral current background (in particular $l^+l^-q\bar{q}$ events, with $l \equiv e, \mu, \tau$) and 0.9 from the WW background.

As the two last procedures (requirement on the total charge of the pair and on the presence of leptons in the pair) each showed good agreement between data and the predictions of the simulation, the results were summed, and the larger of the statistical error of the data and the difference between data and simulation was assumed as a systematic uncertainty. This was estimated to be ±9% on the cross-section measurement.

The uncertainty on the cross-section measurement due to the measurement of the luminosity was evaluated to be ±0.6%.

The total estimated systematic error on the $q\bar{q}q\bar{q}$ $Z\gamma^*$ cross-section measurement was thus estimated to be ±18%.

8 Results for the Matrix Element signal definition

The measurements described in the previous sections 4.1, 5.1.4, 6.2 and 7 show good agreement with the expectations of the Standard Model. Individual cross-sections were extracted by maximizing probability functions with respect to the value of the $Z\gamma^*$ cross-sections: Poissonian probabilities, based on the number of events selected in data and predicted in the simulation, were used for the $q\bar{q}\nu\bar{\nu}$ and $q\bar{q}q\bar{q}$ channels; probability functions derived from fitting procedures were used for the $\mu^+\mu^-q\bar{q}$, $e^+e^-q\bar{q}$ and $l^+l^-l'^+l'^-$ channels. For each centre-of-mass energy, results were expressed in terms of the ratio $R_{Z\gamma^*}$ of measured to expected cross-sections, thus automatically taking into account the (smooth) dependence with energy predicted by the Standard Model. The results obtained for the different energies were first combined for each channel separately, and then into a single value. Global likelihoods were constructed to perform such combinations. The central value was defined as the point of minimum $-log\,L$ distribution and the statistical error as the interval around the central value which contained 68.26% of the probability. The results obtained for the different channels are shown in table 8 and in figure 12. The table also shows the average, luminosity-weighted cross-section for each of the final states considered, predicted by the Standard Model. For completeness, the result obtained for the non-$Z\gamma^*$ contribution to the $e^+e^-q\bar{q}$ final state (see section 4.1) is reported here:

$$R_{non-Z\gamma^*}^{e^+e^-q\bar{q}} = 1.35\ ^{+0.30}_{-0.27}\ ,$$

where the error is statistical only.

21

The systematic uncertainties for each channel were studied by introducing appropriately modified assumptions for backgrounds and efficiencies (as described in the corresponding sections) and were considered as fully correlated between the energies. The effect of systematic uncertainties in the combination of different channels was taken into account as follows: systematic effects were grouped into two categories, depending on whether they were considered as correlated or uncorrelated between the different final states. The correlated uncertainties were those due to the luminosity measurement and to variations in the predicted background cross-sections. Gaussian random numbers were drawn and assigned taking into account the nature of the error (common random numbers among the channels for correlated errors, and independent ones otherwise). The probability functions were then modified accordingly and their combination was repeated a large number of times. The standard deviation of the Gaussian-like distribution of central values obtained was taken to represent the total systematic error affecting the combined measurement.

The final result for the Matrix Element signal definition was

$$R_{Z\gamma^*} \ = \ 1.04 \ ^{+0.13}_{-0.12}(stat) \ \pm \ 0.04(syst) \ ,$$

for $|cos\theta_{f^\pm}| < 0.98$, as shown in table 8 and in figure 12. This result is in good agreement with the Standard Model expectation.

channel	$R_{Z\gamma^*}$	$\bar{\sigma}_{SM}$ (pb)
$\mu^+\mu^- q\bar{q}$	$0.98^{+0.21}_{-0.19} \pm 0.05$	0.11
$e^+e^- q\bar{q}$	$1.05^{+0.33}_{-0.22} \pm 0.08$	0.11
$q\bar{q}\nu\bar{\nu}$	$1.05^{+0.22}_{-0.21} \pm 0.09$	0.08
$l^+l^-l'^+l'^-$	$1.28^{+0.69}_{-0.54} \pm 0.10$	0.03
$q\bar{q}q\bar{q}$	$1.09^{+0.60}_{-0.47} \pm 0.18$	0.29
Total	$1.04^{+0.13}_{-0.12} \pm 0.04$	0.64

Table 8: Ratios of measured to predicted cross-sections, using the Matrix Element signal definition, for individual channels contributing to the $Z\gamma^*$ process. The first errors are statistical and the second systematic. In the last column $\bar{\sigma}_{SM}$(pb) is the average, luminosity-weighted $Z\gamma^*$ cross-section predicted by the Standard Model.

Table 9 and figure 13 show the results at the various energy points, averaged over the different channels.

8.1 Results for the LEP signal definition

The same procedures as described in the previous section were applied in order to obtain results for the $Z\gamma^*$ cross-sections with the LEP signal definition. The final results for the three channels used are summarised in table 10. A combined value of

$$\sigma_{Z\gamma^*} \ = \ 0.137 \ ^{+0.029}_{-0.026}(stat) \ \pm \ 0.014(syst) \ \text{pb}$$

was obtained for the luminosity-weighted cross-section with the LEP signal definition.

E (GeV)	$R_{Z\gamma^*}$	σ_{SM} (pb)
182.7	$1.55^{+0.54}_{-0.46} \pm 0.04$	0.74
188.6	$0.83^{+0.27}_{-0.23} \pm 0.04$	0.69
191.6	$0.41^{+0.58}_{-0.17} \pm 0.04$	0.67
195.5	$1.18^{+0.47}_{-0.39} \pm 0.04$	0.66
199.5	$0.89^{+0.43}_{-0.35} \pm 0.04$	0.65
201.6	$2.63^{+0.88}_{-0.74} \pm 0.04$	0.63
205.0	$1.52^{+0.56}_{-0.49} \pm 0.04$	0.59
206.5	$0.44^{+0.24}_{-0.20} \pm 0.04$	0.57
Average	$1.04^{+0.13}_{-0.12} \pm 0.04$	0.64

Table 9: Ratios of measured to predicted cross-sections, using the Matrix Element signal definition, averaged over the different channels at the various energy points. The first errors are statistical and the second systematic. The last column shows the Standard Model predictions.

channel	σ (pb)	$\bar{\sigma}_{SM}$ (pb)
$\mu^+\mu^- q\bar{q}$	$0.031^{+0.013}_{-0.011} \pm 0.004$	0.042
$e^+e^- q\bar{q}$	$0.063^{+0.018}_{-0.016} \pm 0.009$	0.058
$q\bar{q}\nu\bar{\nu}$	$0.042^{+0.022}_{-0.020} \pm 0.008$	0.051
Total	$0.137^{+0.029}_{-0.026} \pm 0.014$	0.151

Table 10: Luminosity-weighted cross-sections for individual channels contributing to the $Z\gamma^*$ process measured with the LEP signal definition (see section 2). The first errors are statistical and the second systematic. In the last column $\bar{\sigma}_{SM}$(pb) is the average, luminosity-weighted $Z\gamma^*$ cross-section predicted by the Standard Model.

9 Conclusions

In the data sample collected by the DELPHI detector at centre-of-mass energies ranging from 183 GeV to 209 GeV, the values of the $Z\gamma^*$ cross-section contributing to the four-fermion final states $\mu^+\mu^- q\bar{q}$, $e^+e^- q\bar{q}$, $l^+l^-l^+l^-$, $q\bar{q}\nu\bar{\nu}$ and $q\bar{q}q\bar{q}$ with $|cos\theta_{f^\pm}| < 0.98$ have been measured and compared with Standard Model expectations. A combined value of

$$R_{Z\gamma^*} = 1.04 ^{+0.13}_{-0.12}(stat) \pm 0.04(syst)$$

was obtained for the Matrix Element signal definition, in good agreement with the Standard Model predictions.

Additional cross-section measurements in the channels $\mu^+\mu^- q\bar{q}$, $e^+e^- q\bar{q}$ and $q\bar{q}\nu\bar{\nu}$ were performed using the common LEP signal definition. A combined, luminosity-weighted, value of

$$\sigma_{Z\gamma^*} = 0.137 ^{+0.029}_{-0.026}(stat) \pm 0.09(syst) \text{ pb}$$

was obtained, in good agreement with the Standard Model prediction of 0.151 pb.

10   Acknowledgements

References

[1] K. Hagiwara, R.D. Peccei, D. Zeppenfeld and K.Hikasa, Nucl. Phys. **B282** (1987) 253.

[2] ALEPH Collaboration, R. Barate *et al.*, Phys. Lett. **B484** (2000) 205;
DELPHI Collaboration, P. Abreu *et al.*, Phys. Lett. **B479** (2000) 89;
L3 Collaboration, M. Acciarri *et al.*, Phys. Lett. **B496** (2000) 19;
OPAL Collaboration, G. Abbiendi *et al.*, Phys. Lett. **B493** (2000) 249.

[3] ALEPH Collaboration, R. Barate *et al.*, Phys. Lett. **B469** (1999) 287;
DELPHI Collaboration, P. Abreu *et al.*, Phys. Lett. **B497** (2001) 199;
L3 Collaboration, M. Acciarri *et al.*, Phys. Lett. **B497** (2001) 23;
OPAL Collaboration, G. Abbiendi *et al.*, Phys. Lett. **B476** (2000) 256.

[4] DELPHI Collaboration, P. Aarnio *et al.*, Nucl. Instr. and Meth. **A303** (1991) 233.

[5] DELPHI Collaboration, P. Abreu *et al.*, Nucl. Instr. and Meth. **A378** (1996) 57.

[6] DELPHI Silicon Tracker Group, P. Chochula *et al.*, Nucl. Instr. and Meth. **A412** (1998) 304.

[7] E. Accomando and A. Ballestrero, Comp. Phys. Comm. **99** (1997) 270;
E. Accomando, A. Ballestrero and E. Maina, hep-ph/0204052 (2002).

[8] A. Ballestrero, R. Chierici, F. Cossutti and E. Migliore, CERN-EP 306 (2002), accepted by Comp. Phys. Comm.

[9] T. Sjöstrand *et al.*, Comp. Phys. Comm. **135** (2001) 238.

[10] S. Jadach *et al.*, Phys. Lett. **B417** (1998) 326;
W. Beenakker, F.A. Berends and A.P. Chapovski, Nucl. Phys. **B548** (1999) 3.

[11] A. Denner *et al.*, Nucl. Phys. **B587** (2000) 67.

[12] S. Jadach *et al.*, Comp. Phys. Comm. **140** (2001) 432.

[13] Y. Kurihara, J. Fujimoto, T. Munehisha and Y. Shimizu, Prog. Theor. Phys. **96** (1996) 1223.

[14] M. Boonekamp, DAPNIA-SPP-01-16, hep-ph/0111213, (2001).

[15] S. Jadach, B.F.L. Ward and Z. Was, Comp. Phys. Comm. **130** (2000) 260.

[16] S. Jadach, W. Placzek and B.F.L. Ward, Phys. Lett. **B390** (1997) 298.

[17] F.A. Berends, P.H. Daverveldt and R. Kleiss, Comp. Phys. Comm. **40** (1986) 271, 285, 309.

[18] T. Sjöstrand, `PYTHIA 5.7` *and* `JETSET 7.4`, CERN-TH/7112/93 (1993).

[19] F.A. Berends, R. Pittau and R. Kleiss, Comp. Phys. Comm. **85** (1995) 437.

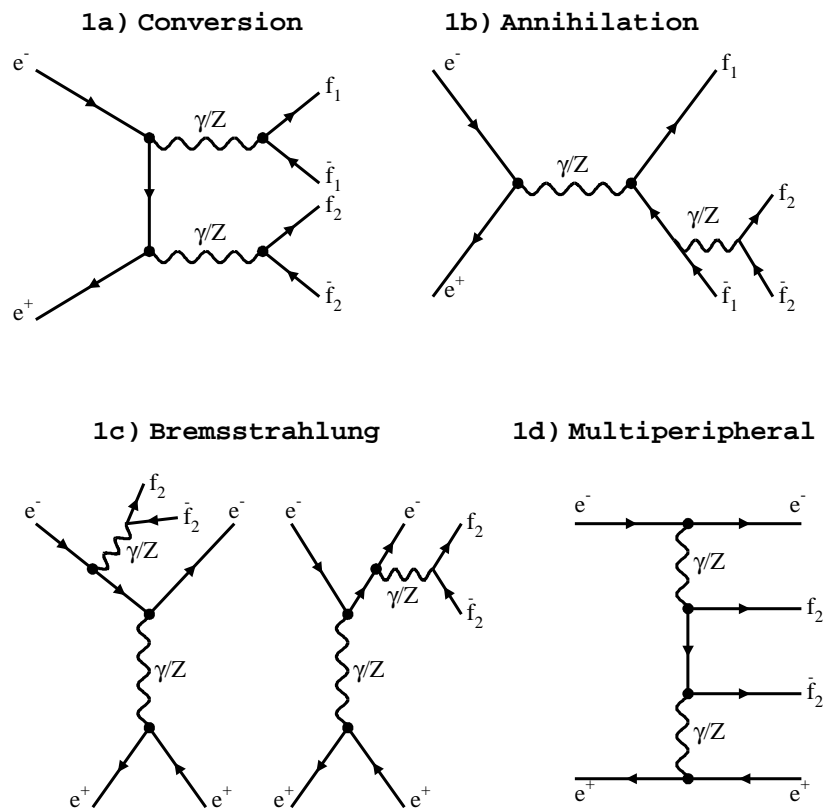[20] S. Jadach *et al.*, Comp. Phys. Comm. **119** (1999) 272.

Figure 1: The Feynman diagrams for four-fermion neutral current production in e^-e^+ collisions.
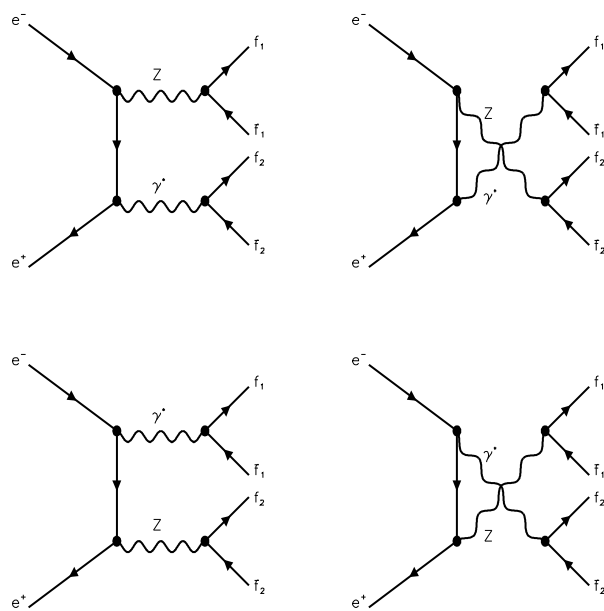
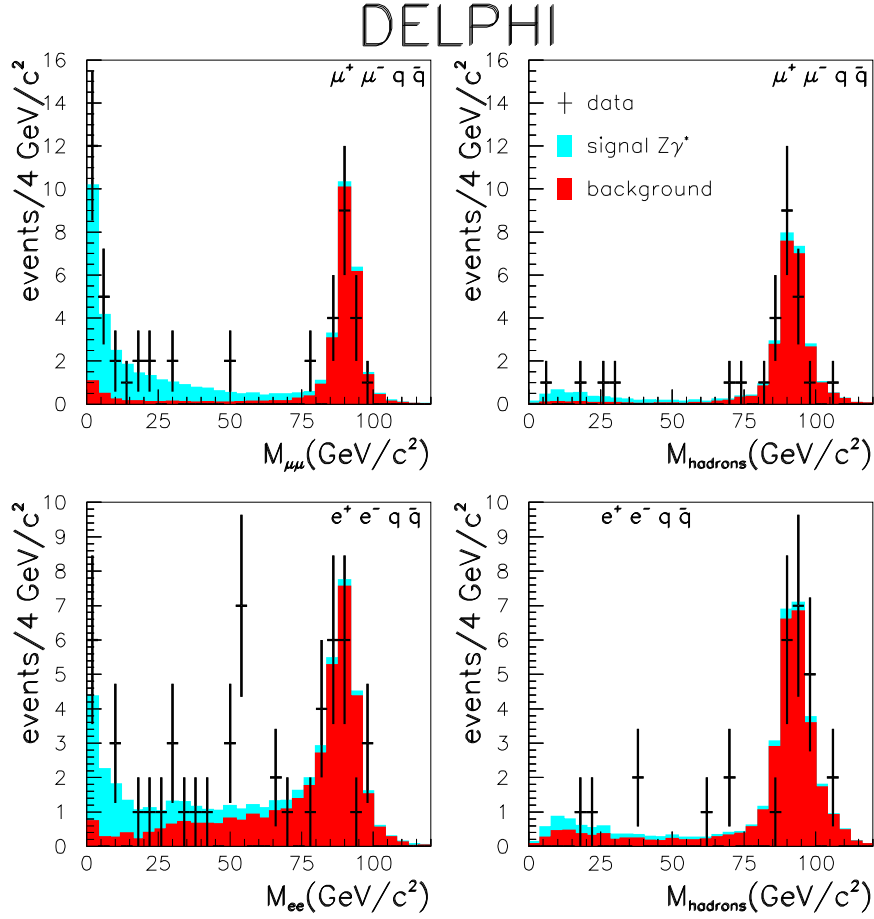Figure 2: Neutral current conversion diagrams for the $Z\gamma^*$ process.

Figure 3: $l^+l^-q\bar{q}$ final state: Distributions of the mass of one fermion pair when the mass of the second is within 15 GeV$/c^2$ of M_Z. The two lower plots are for the $e^+e^-q\bar{q}$ channel and the two upper plots for the $\mu^+\mu^-q\bar{q}$ channel. The points are the data, the dark (red) histogram is the distribution of the background predicted by the Standard Model, and the light (light blue) histogram is the predicted distribution of the $Z\gamma^*$ signal. The Matrix Element signal definition has been used here.
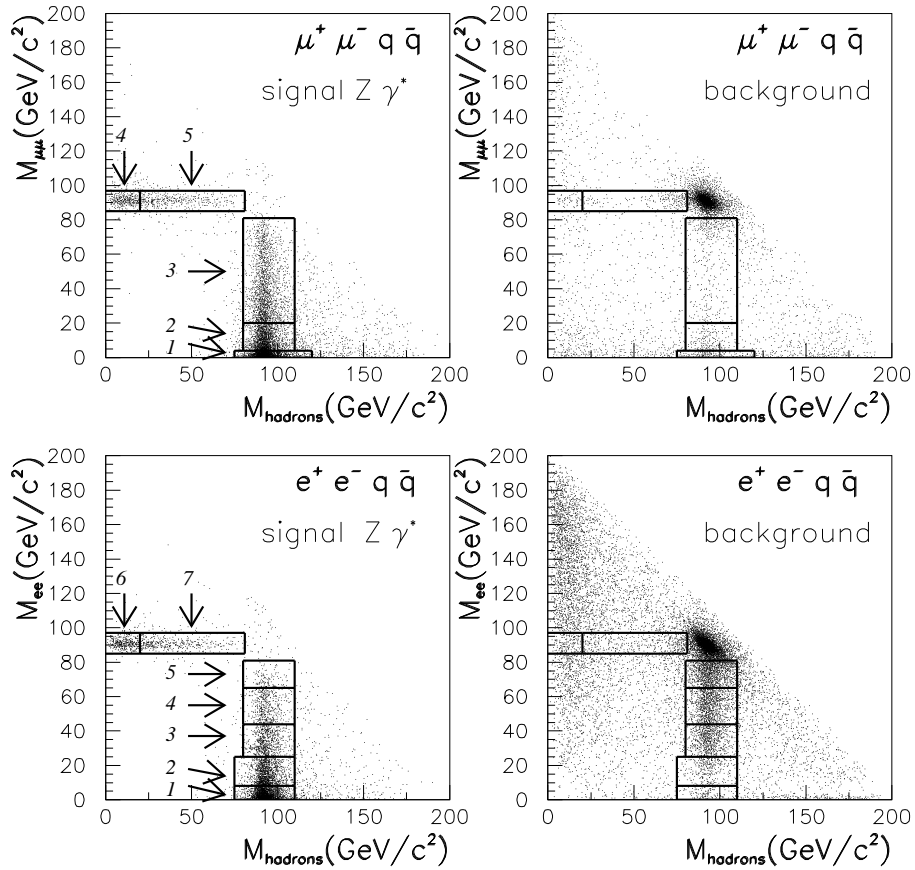
Figure 4: $l^+l^-q\bar{q}$ final state: Bidimensional distributions in the plane of the di-fermion masses predicted by the Standard Model for signal $Z\gamma^*$ (left-hand plots) and background (right-hand plots) for the two channels studied. The bins used for the fit are also shown. The Matrix Element signal definition has been used here.
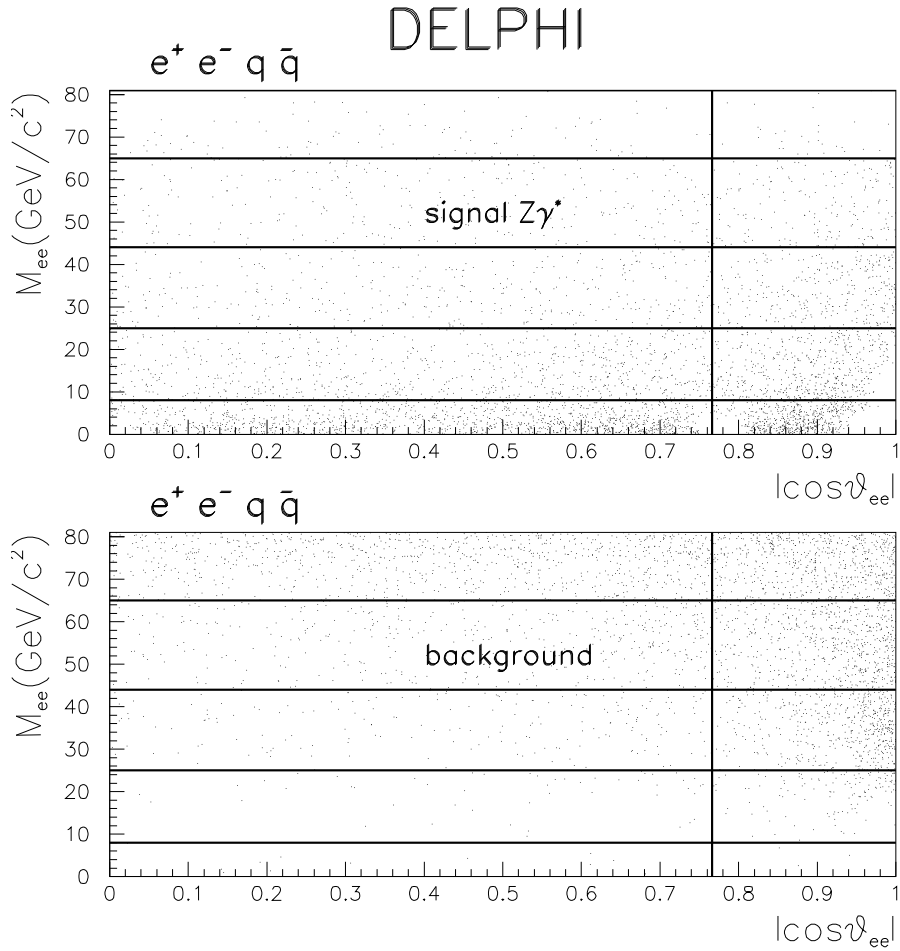
Figure 5: Distributions of the mass of the electron-positron pair in $e^{+}e^{-}q\bar{q}$ events versus the polar direction of the pair for signal $Z\gamma^{*}$ (upper plot) and background (lower plot) when the mass of the hadronic system is compatible with the Z mass. The plot shows the predictions of the Standard Model. The binning adopted for these events is also indicated on the plots. The Matrix Element signal definition has ben used here.
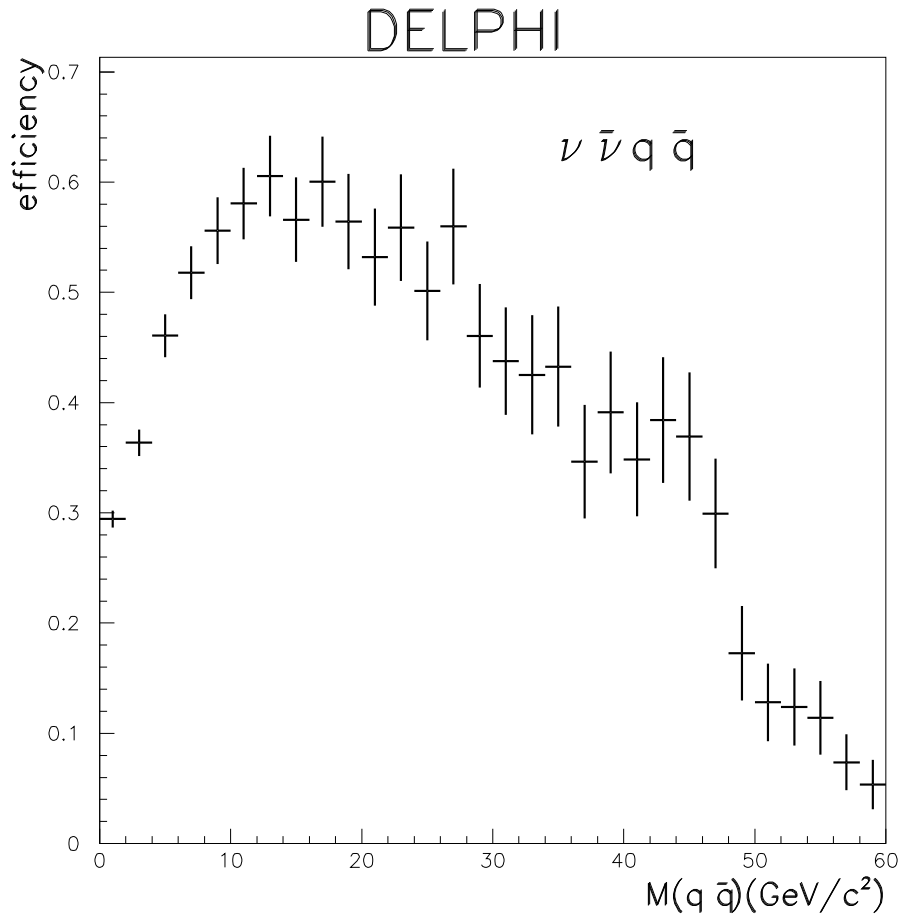
Figure 6: Results for $\mu^+\mu^- q\bar{q}$ (upper plot) and $e^+e^- q\bar{q}$ (lower plots). The points are data; the shaded histograms show the results of fits to the $Z\gamma^*$ component ($\mu^+\mu^- q\bar{q}$), or to the $Z\gamma^*$ and non-$Z\gamma^*$ components ($e^+e^- q\bar{q}$), and the predicted Standard Model contributions from other sources. See figures 4 and 5 for the bin definitions. The Matrix Element signal definition has been used here.

31

Figure 7: Combined selection efficiency of the $q\bar{q}\nu\bar{\nu}$ analysis as a function of the generated $M(q\bar{q})$ mass. The Matrix Element signal definition is here used.
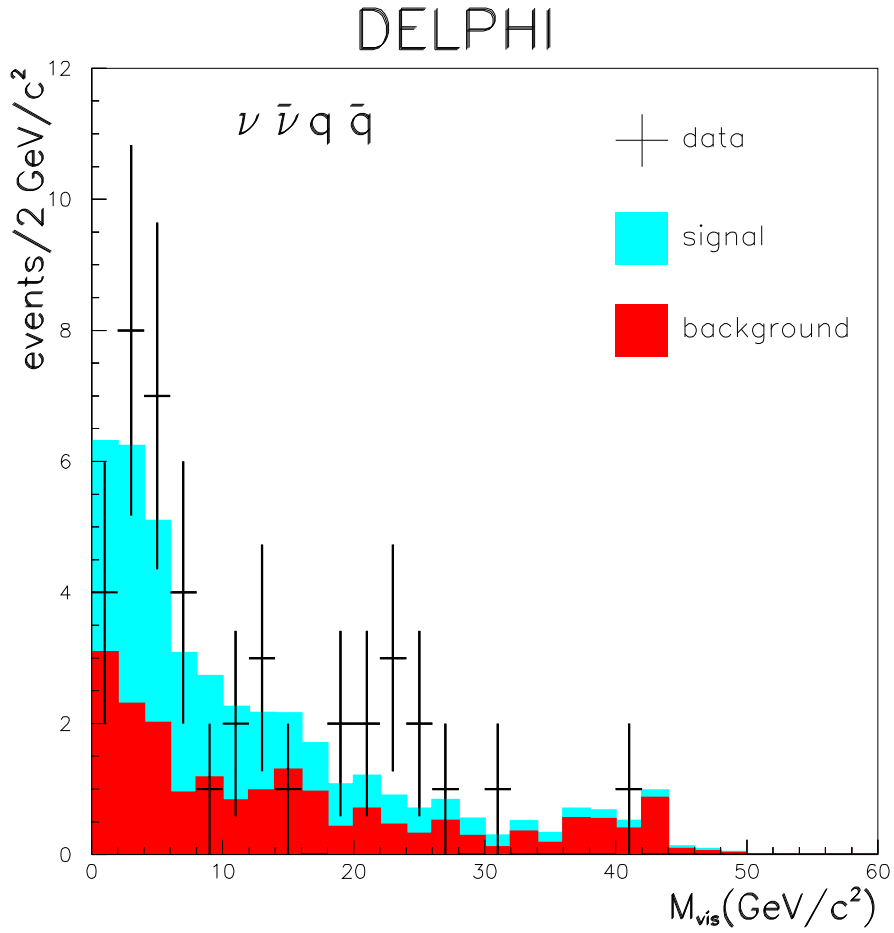
Figure 8: Distribution of the visible invariant mass of the hadronic system in the $q\bar{q}\nu\bar{\nu}$ selection, compared with the Standard Model predictions for signal and background. The points are the data, the light (light blue) histogram shows the predicted signal contribution, and the dark (red) histogram shows the predicted background. The Matrix Element signal definition has been used here.
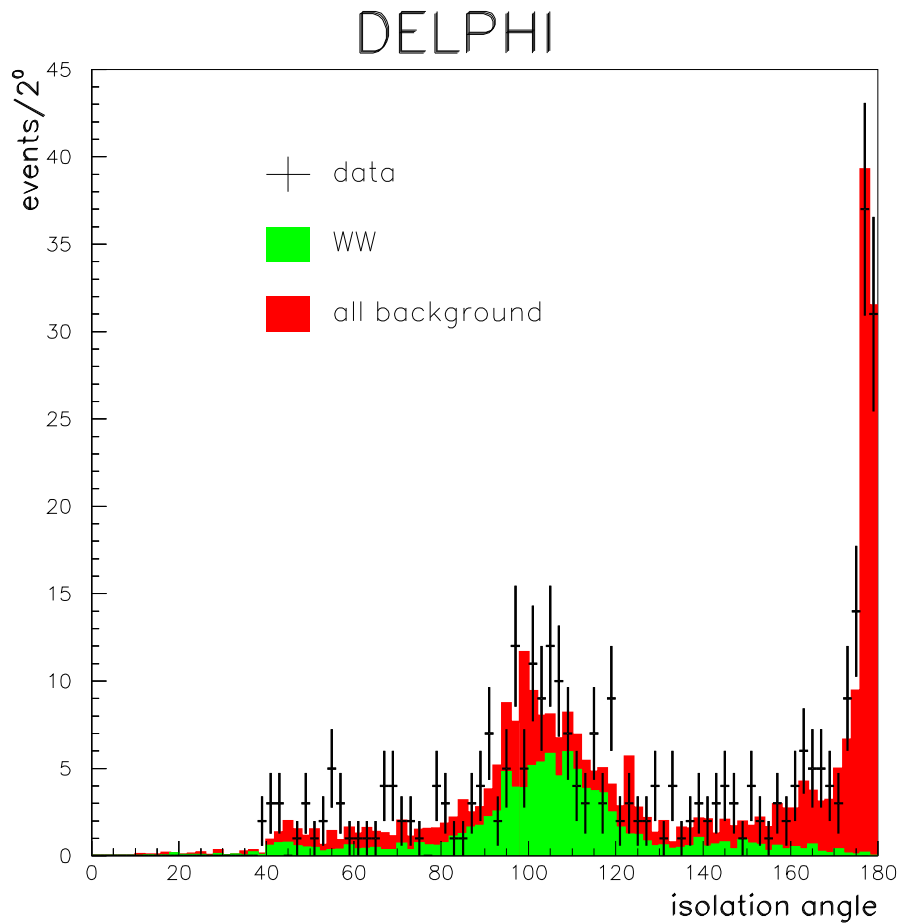
Figure 9: Isolation angle of selected electrons, muons and single charged particle tracks in the sample selected to mimic the background to the selected $q\bar{q}\nu\bar{\nu}$ sample. The points are data, the light (green) histogram is the predicted WW contribution, the dark (red) histogram is the rest of the background.
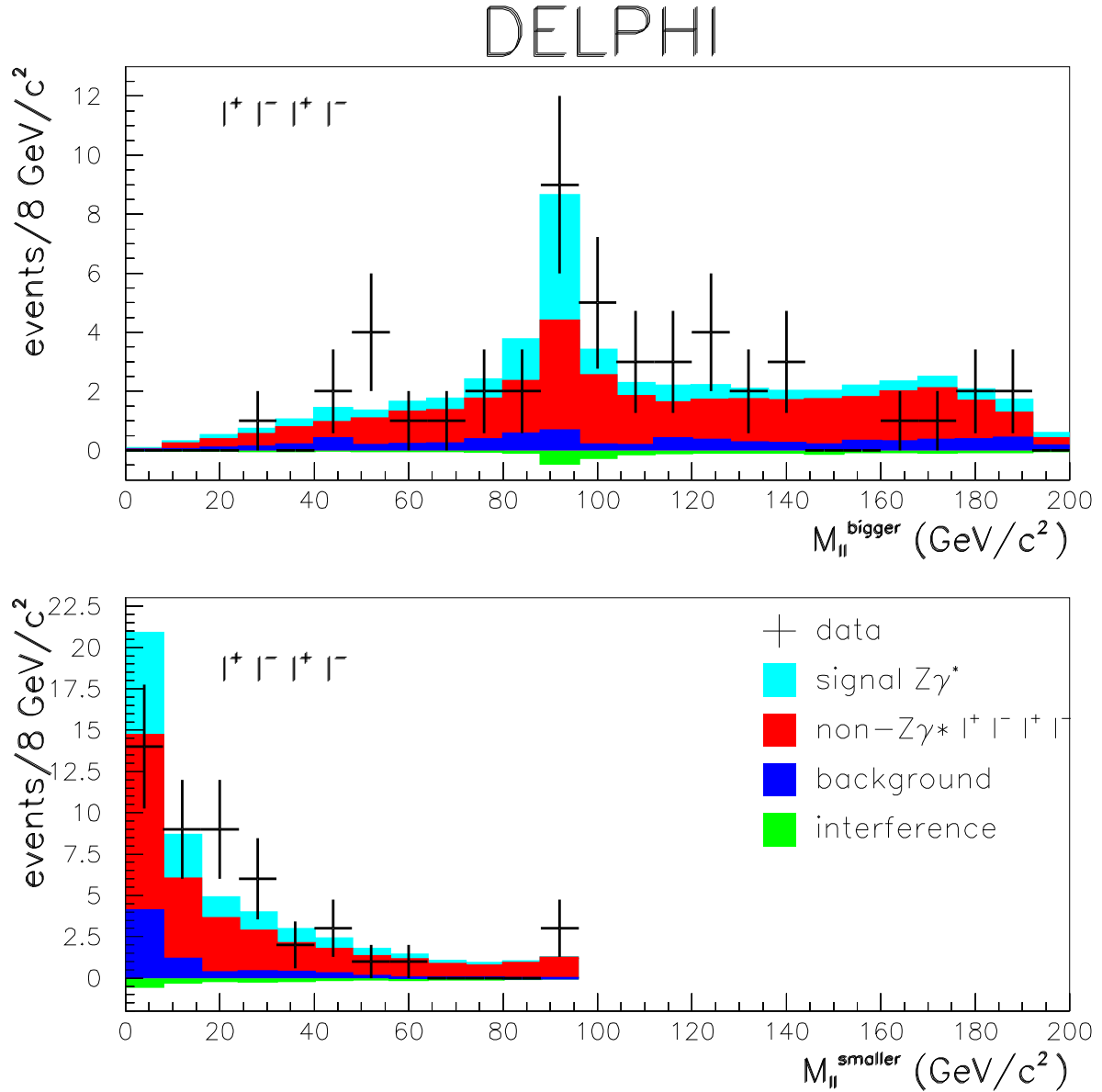
Figure 10: Four-lepton channel: Fitted masses of two selected lepton pairs: bigger mass (top plot), smaller mass (bottom plot), compared with Standard Model predictions. The points are the data and the histograms the predicted contributions to the selected event sample. In the legend, "background" means the contribution from non-$l^+l^-l'^+l'^-$ final states.
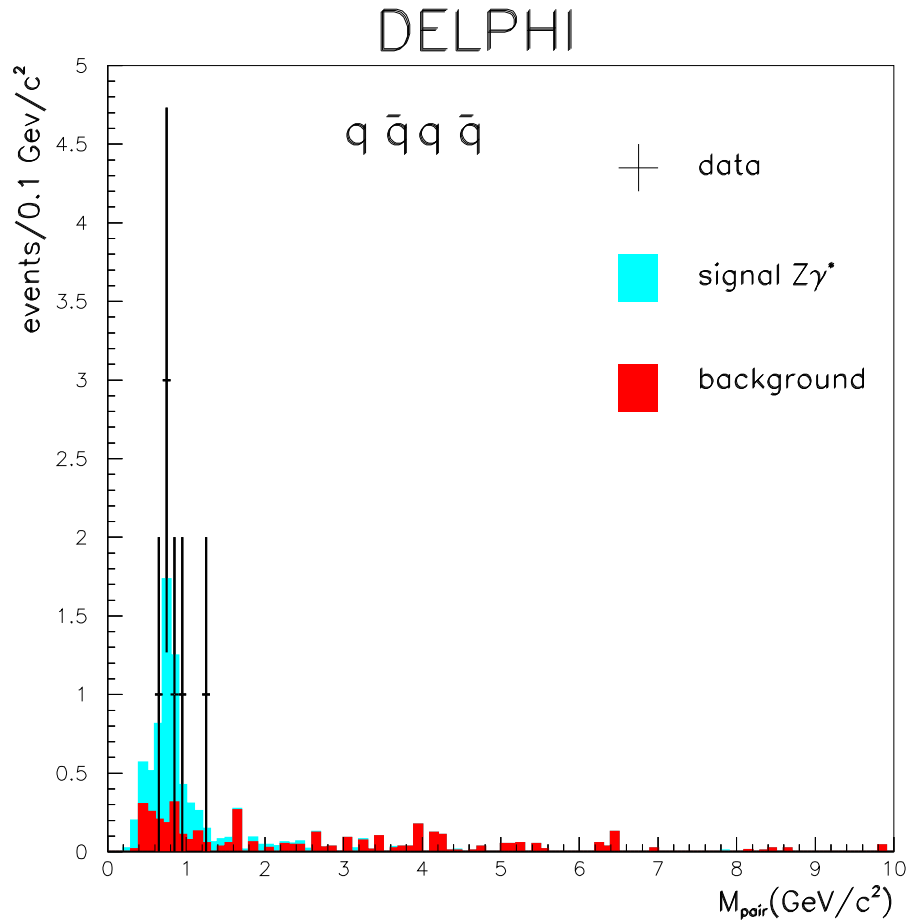
Figure 11: The distribution of the reconstructed invariant mass of the selected pair of charged tracks in the $q\bar{q}q\bar{q}$ analysis, compared with the predictions of the Standard Model. The points are data, the light (green) histogram shows the predicted $Z\gamma^*$ contribution, and the dark (red) histogram shows the predicted background.
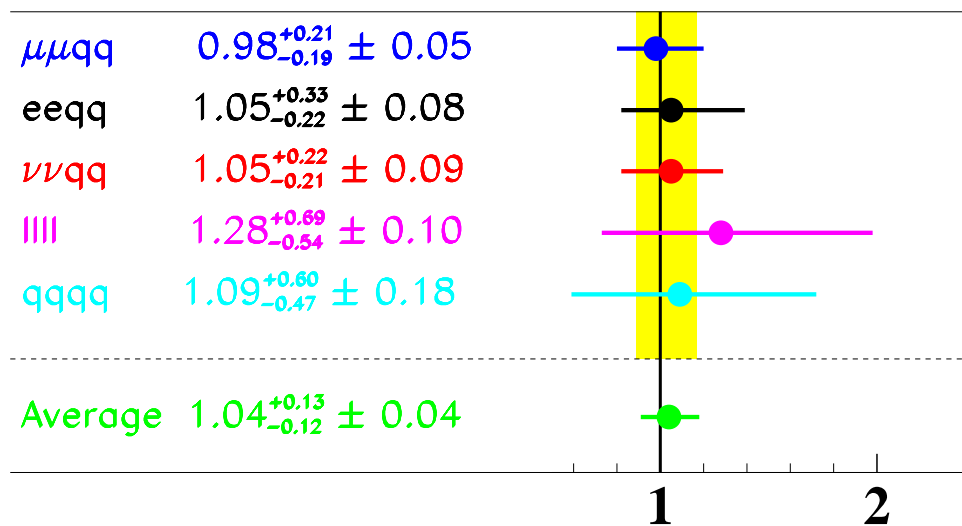
Figure 12: Ratios of measured to predicted cross-sections, using the Matrix Element signal definition, for individual channels contributing to the $Z\gamma^*$ process. The vertical band displays the total error on the combination of the channels.
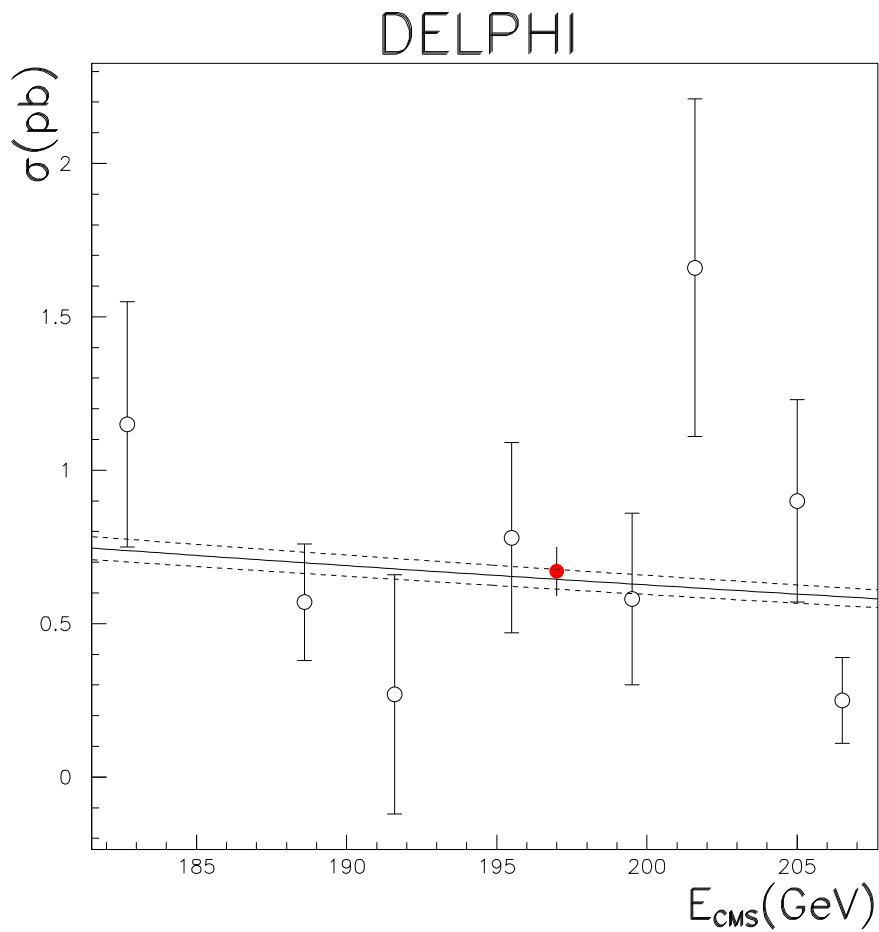
Figure 13: Combined $Z\gamma^*$ cross-sections, using the Matrix Element signal definition, as a function of the centre-of-mass energy. The solid line is the Standard Model prediction; the dashed line represents a 5% uncertainty around this prediction.The full (red) point is the average cross-section result, plotted on the luminosity weighted average centre-of-mass energy.